Towards Coupled Nonhydrostatic-Hydrostatic Hybridizable Discontinuous Galerkin Method

by

Aditya Karthik Saravanakumar

Submitted to the Center for Computational Science and Engineering
in partial fulfillment of the requirements for the degree of

Master of Science in Computational Science and Engineering

at the

MASSACHUSETTS INSTITUTE OF TECHNOLOGY

June 2023

Author ....
Center for Computational Science and Engineering
May 24, 2023

Certified by..
Pierre F.J. Lermusiaux
Professor, Department of Mechanical Engineering
Thesis Supervisor

Accepted by ....
Youssef M. Marzouk
Co-Director, Center for Computational Science and Engineering

Towards Coupled Nonhydrostatic-Hydrostatic Hybridizable Discontinuous Galerkin Method

by

Aditya Karthik Saravanakumar

Submitted to the Center for Computational Science and Engineering
on May 24, 2023, in partial fulfillment of the
requirements for the degree of
Master of Science in Computational Science and Engineering

Abstract

Numerical modelling of ocean physics is essential for multiple applications such as scientific inquiry and climate change but also renewable energy, transport, autonomy, fisheries, water, harvesting, tourism, communication, conservation, planning, and security. However, the wide range of scales and interactions involved in ocean dynamics make numerical modelling challenging and expensive. Many regional ocean models resort to a hydrostatic (HS) approximation that significantly reduces the computational burden. However, a challenge is to capture and study local ocean phenomena involving complex dynamics over a broader range of scales, from regional to small scales, and resolving nonlinear internal waves, subduction, and overturning. Such dynamics require multi-resolution non-hydrostatic (NHS) ocean models. It is known that the main computational cost for NHS models arises from solving a globally coupled elliptic PDE for the NHS pressure. Optimally reducing these costs such that the NHS dynamics are resolved where needed is the motivation for this work.

We propose a new multi-dynamics model to decompose a domain into NHS and HS dynamic regions and solve the corresponding models in their subdomains, reducing the cost associated with the NHS pressure solution step. We extend a high-order NHS solver developed using the hybridizable discontinuous Galerkin (HDG) finite element methodology by taking advantage of the local and global HDG solvers for combining HS with NHS solvers. The multi-dynamics is derived, and the first version is implemented in the HDG framework to quantify computational costs and evaluate accuracy using several analyses. We first showcase results on Rayleigh Taylor instability-driven striations to evaluate computational savings and accuracy compared to the standard NHS HDG and finite-volume solvers. We highlight and discuss sensitivities and performance. Finally, we explore parameters that can be used to identify domain regions exhibiting NHS behaviour, allowing the algorithm to dynamically evolve the NHS and HS subdomains.

Thesis Supervisor: Pierre F.J. Lermusiaux
Title: Professor, Department of Mechanical Engineering

Acknowledgments

I am extremely grateful to my advisor, Prof. Pierre Lermusiaux, for his mentorship and support over the last two years at MIT. I have always found your amazing work ethic and dedication to the research we do at MSEAS to be very inspiring. Thanks for giving me the opportunity to join our lab and for guiding me towards becoming a better researcher.

The daunting task of moving away from home to another country for grad school was made effortless by the incredibly welcoming people here at MSEAS. I feel so lucky to have the privilege of working in this lab and forming many great friendships. I sincerely appreciate the exceptional group dynamic at MSEAS that is very conducive to generating research ideas and this thesis would not be possible without it. The senior members of the lab, Corbin, Manan, Wael, and Aaron, you guys have been a great support system throughout and amazing company and you will be sorely missed once you graduate. A special mention to Corbin for being a great mentor and friend and for helping me through the "shallow" learning curve that comes with HDG. Anantha, Tony, Alonso and Ellery, it has been an absolute pleasure getting to know you guys and I am excited to continue working with you. Chris and Pat, you guys are so dependable and willing to help out all the time, so thanks a lot for that. Kate Nelson and Lisa Maxwell have helped me out with administrative processes time and again to ensure the smooth sailing of my program and I am indebted to them.

I would also like to thank all my friends, in and out of MIT, who have made the last couple of years in grad school so enjoyable and fun. Finally, the unwavering love, encouragement and support I receive from my family is an integral part of what keeps me going and happy so I extend my special gratitude to Amma, Appa and Kailash.

We are grateful to the Office of Naval Research for partial support under grants N00014-18-1-2781 (DRI-CALYPSO) and N00014-19-1-2693 (IN-BDA). We also thank the MIT Portugal Program for support under a MPP seed project and a Flagship program project (K2D).

Contents

List of Figures

List of Tables

Chapter 1

Introduction

Applications of numerical modelling of ocean physics range from scientific inquiry and global climate change to renewable energy, autonomy, fisheries, path planning and environmental conservation. Over the last few decades, the exponential increase in computational power and the emergence of novel numerical methods have led to significant advances in ocean modelling [24, 23, 90, 89]. Yet, accurate numerical simulations of large-scale three-dimensional ocean problems are often prohibitively computationally expensive. Therefore, methods to optimize these simulations and make them more computationally tractable are currently a subject of active research.

The multi-scale interactions associated with ocean dynamics make numerical modelling challenging and expensive. Most regional ocean models employ a hydrostatic (HS) approximation [49, 15] that significantly reduces the computational burden. The validity of the hydrostatic approximation relies on the fact that for typical ocean processes, the aspect ratio, defined as the ratio of the vertical to the horizontal scale of the motion, is very small. However, this approximation breaks down when the aspect ratio becomes substantial, and this limits hydrostatic models from being able to capture and study complex non-hydrostatic (NHS) ocean phenomena.

Non-hydrostatic phenomena [37, 97], such as nonlinear internal waves [110, 45], subduction and overturning, are believed to be the link between the slow-moving large-scale motions and the high-speed mixing scales in the ocean [34]. Such NHS behaviour, in the form of nonlinear internal solitary waves, was observed in the Luzon Strait and South China Sea [10]. Some low-order ocean models [11, 48, 52, 69] with non-hydrostatic capability include the SUNTANS [35], the MIT GCM [72], PSOM [70, 71], Oceananigans [91], MERF v3.0 [100], FVCOM [55, 56] and CROCO-ROMS [86, 96]. Over the last few decades, high-order methods [54] have emerged as candidates for non-hydrostatic ocean modelling but are still nascent. A Hybridizable Discontinuous Galerkin (HDG) [77, 78] discretization scheme based on the pressure-projection method [16, 101, 6] for the incompressible Navier-Stokes and non-hydrostatic ocean equations were presented in [103, 106]. This model has also been extended to study biological processes in regions such as Stellwagen Bank in Massachusetts [104, 102, 107]. More recently, a Discontinuous Galerkin multi-layered non-hydrostatic coastal ocean model was presented in [82, 83].

Typically, non-hydrostatic ocean models are based on the pressure decomposition proposed in [12], which splits the pressure into a sum of hydrostatic and non-hydrostatic components. This results in a globally coupled three-dimensional pressure-Poisson equation (PPE) to be solved to compute the non-hydrostatic pressure component. However, for large-scale ocean problems, this PPE is poorly conditioned because the vertical and horizontal second-derivative terms are typically two orders of magnitudes apart [35, 111], drastically increasing the computational cost. Furthermore, it is understood [110] that accurate simulations of non-hydrostatic effects come with a significant horizontal resolution requirement that might be beyond the reach the current state-of-the-art ocean solvers.

1.1 Present Research

In this thesis, as a method to mitigate the computational challenge posed by NHS simulations, we start developing a multi-dynamics algorithm to decompose a domain into NHS and HS dynamic regions and solve the corresponding models in their subdomains, thereby reducing the cost associated with the NHS pressure solution step. We take a look at the advantages and disadvantages of different coupling approaches for the NHS and HS subdomains before presenting our novel projection-method-based coupling strategy. Implementation details are explained while addressing key questions related to communication between subdomains and boundary condition treatment at the subdomain interfaces. We then explore parameters that can be used to identify domain regions exhibiting NHS behaviour, allowing the algorithm to change the NHS and HS subdomains dynamically. Finally, we show results from a first implementation of this algorithm on an idealized test case to quantify computational costs, evaluate the accuracy, and compare against the standard NHS HDG and finite-volume solvers.

Some of the questions that motivate our research include: Could we use and interconnect different models in different regions based on the local dynamics in these regions? How could we accurately couple these modeling subdomains with different dynamics? What are the correct boundary conditions and global dynamical effects across such multi-dynamics interconnected subdomains? What are ideal schemes and implementations for facilitating communication among subdomains that employ different governing equations and solvers? Can we find and employ specific parameters to anticipate and predict the local dynamics of subdomains? Using these parameters, can we adapt the equations used in the subdomains dynamically? When do multi-dynamics solvers become inefficient, e.g., when should the most complex dynamics be used everywhere? In what follows, we will start to address some of the questions.

1.2 Thesis Outline

Here we describe the outline of the thesis with a synopsis of each chapter for the sake of the reader's convenience.

- *Chapter 1 - Introduction*: A brief introduction to the application of numerical modelling for ocean dynamics highlighting the current state of research and motivation for this thesis.

- *Chapter 2 - Numerical Methods for Ocean Modelling*: An overview of the derivation of the hydrostatic and non-hydrostatic ocean equations followed by a discussion on the pressure-projection method and the HDG framework.

- *Chapter 3 - Multi-Dynamics model*: Methods to improve NHS solver efficiency are discussed, and the proposed multi-dynamics algorithm is derived with attention to implementation details.

- *Chapter 4 - Numerical Investigation*: An idealized test case of Rayleigh -Taylor-instability driven striation is used to conduct numerical experiments that implement the multi-dynamics model and estimate accuracy and computational savings.

- *Chapter 5 - Conclusion and Future Work*: Results from this thesis are summarized and possible extensions of this work are examined.

Chapter 2

Numerical Methods for Ocean Modelling

The non-linear and anisotropic nature of ocean dynamics makes ocean modelling a challenging endeavour. The scales associated with ocean phenomena can range from seconds to geological time scales and meters to thousands of kilometres. Historically, finite volume methods have been the popular choice for ocean modelling and computational fluid dynamics (CFD) in general. However, finite element methods offer tools for tackling large-scale multi-resolution simulations on unstructured grids in a computationally tractable fashion. A finite element method with unstructured grid capabilities was used for non-hydrostatic modelling for the first time in [29] and later extended to accommodate a free-surface in [87]. Over the last couple of decades, Discontinuous Galerkin (DG) finite element methods have gained popularity in the CFD community. These methods offer high-order accuracy on unstructured grids and are well-suited for modern-day parallel computing. DG finite element methods have been applied to hydrostatic models in the context of the shallow water equations with success in [24, 23] and other ocean and lake dynamics [108, 94, 43, 26]. We refer to [44] for an introduction to DG methods.

In this chapter, we review the non-hydrostatic and hydrostatic forms of the ocean dynamics equations and discuss the projection method used to solve the two sets of equations as described in [103]. We then provide a brief overview of the hybridizable

Discontinuous Galerkin (HDG) finite element method and its application to such ocean dynamics.

2.1 Ocean Dynamics Equations

The equations governing ocean dynamics, also known as the primitive equations (PE), are derived from the Navier-Stokes equations augmented with Coriolis forcing along with transport equations for temperature and salinity, and an equation of state [20]. It's also common to consider a density decomposition based on the *Boussinesq approximation* which is rooted in the fact that density variations in the ocean are typically small in magnitude ($\approx 1\%$). The density is split into a constant mean density ρ_0 and a spatially and temporally varying perturbation as

$$\rho(\underline{x}, t) = \rho_0 + \rho'(\underline{x}, t) \qquad \text{where} \qquad |\rho'(\underline{x}, t)| \ll \rho_0 \tag{2.1}$$

Since typical ocean processes possess vastly different length scales and time scales along the vertical and horizontal directions, we define the state variables as the horizontal velocities $\underline{u} = [u, v, 0]$, vertical velocity $\underline{w} = [0, 0, w]$, pressure p, density ρ, temperature T and salinity S. Using the Boussinesq approximation and an eddy-viscosity closure model we can write the governing equations as [103].

$$\frac{\partial \underline{u}}{\partial t} + \nabla_{xy} \cdot \underline{u}\,\underline{u} + \nabla_z \cdot \underline{w}\,\underline{u} = - \frac{1}{\rho_0}\nabla_{xy}p + \nabla_{xy} \cdot \nu_{xy}\nabla_{xy}\underline{u} \tag{2.2}$$

$$+ \nabla_z \cdot \nu_z \nabla_z \underline{u} - f\hat{k} \times \underline{u} + \frac{1}{\rho_0}\underline{f_u}$$

$$\frac{\partial \underline{w}}{\partial t} + \nabla_{xy} \cdot \underline{u}\,\underline{w} + \nabla_z \cdot \underline{w}\,\underline{w} = - \frac{1}{\rho_0}\nabla_{z}p + \nabla_{xy} \cdot \nu_{xy}\nabla_{xy}\underline{w} \tag{2.3}$$

$$+ \nabla_z \cdot \nu_z \nabla_z \underline{w} + \frac{\rho}{\rho_0}\underline{g} + \frac{1}{\rho_0}\underline{f_w}$$

$$\nabla_{xy} \cdot \underline{u} + \nabla_z \cdot \underline{w} = 0 \tag{2.4}$$

$$\frac{\partial T}{\partial t} + \nabla_{xy} \cdot \underline{u}T + \nabla_z \cdot \underline{w}T = \nabla_{xy} \cdot \kappa_{xy}\nabla_{xy}T + \nabla_z \cdot \kappa_z \nabla_z T + f_T, \tag{2.5}$$

$$\frac{\partial S}{\partial t} + \nabla_{xy} \cdot \underline{u}S + \nabla_z \cdot \underline{w}S = \nabla_{xy} \cdot \kappa_{xy}\nabla_{xy}S + \nabla_z \cdot \kappa_z \nabla_z S + f_S \tag{2.6}$$

$$\rho = \rho(S, T) \tag{2.7}$$

where the divergence operators are defined as $\nabla_{xy} = \left[\frac{\partial}{\partial x}, \frac{\partial}{\partial y}, 0\right]$ and $\nabla_z = \left[0, 0, \frac{\partial}{\partial z}\right]$. The Coriolis parameter is denoted by f, the gravity vector by $\underline{g} = [0, 0, -g]$ and the turbulent viscosities and diffusivities by $\nu_{xy/z}$ and $\kappa_{xy/z}$.

We now consider a pressure decomposition formulation, as proposed in [12], wherein the pressure field is decomposed into hydrostatic and non-hydrostatic components as

$$p = p_{hyd} + \rho_0 p' \tag{2.8}$$

where the hydrostatic pressure is defined in terms of the density field and free-surface elevation $\eta\,(x, y, t)$ as

$$p_{hyd}\,(x, y, z, t) = \int_z^{\eta(x,y,t)} \rho\,(x, y, \zeta, t)\, g \,\mathrm{d}\zeta \tag{2.9}$$

We note that the vertical gradient of this hydrostatic pressure $\nabla_z p_{hyd} = -g\rho$ exactly cancels the $\frac{\rho}{\rho_0}g$ term in the vertical momentum equation. In a hydrostatic model, this means that the effects of the density forcing are fully captured in the horizontal momentum equations through p_{hyd}.

Introducing this pressure decomposition into the governing equations and adding an equation for the free-surface elevation $\eta(x,y,t)$ to satisfy the kinematic boundary condition at the free surface, we get

$$\begin{aligned}\frac{\partial \underline{u}}{\partial t}+\nabla_{xy}\cdot\underline{u}\,\underline{u}+\nabla_{z}\cdot\underline{w}\,\underline{u}=&-\nabla_{xy}p'-\underline{g}\nabla_{xy}\eta-\frac{1}{\rho_0}\int_z^{\eta}\underline{g}\nabla_{xy}\rho'\mathrm{d}\zeta \qquad (2.10)\\ &+\nabla_{xy}\cdot\nu_{xy}\nabla_{xy}\underline{u}+\nabla_z\cdot\nu_z\nabla_z\underline{u}-f\hat{k}\times\underline{u}+\frac{1}{\rho_0}\underline{f_u}\\ \frac{\partial \underline{w}}{\partial t}+\nabla_{xy}\cdot\underline{u}\,\underline{w}+\nabla_{z}\cdot\underline{w}\,\underline{w}=&-\nabla_{z}p'+\nabla_{xy}\cdot\nu_{xy}\nabla_{xy}\underline{w} \qquad (2.11)\\ &+\nabla\cdot\nu_z\nabla_z\underline{w}+\frac{1}{\rho_0}\underline{f_w}\\ \nabla_{xy}\cdot\underline{u}+\nabla_z\cdot\underline{w}=&0 \qquad (2.12)\\ \frac{\partial\eta}{\partial t}+\nabla_{xy}\cdot\int_{-H}^{\eta}\underline{u}\mathrm{d}z=&0 \qquad (2.13)\end{aligned}$$

which we will henceforth refer to, along with Eqs.2.5-2.6, as the non-hydrostatic (NHS) ocean equations. From this, we can derive the hydrostatic (HS) equations by setting $p'\approx 0$, which leads to

$$\begin{aligned}\frac{\partial \underline{u}}{\partial t}+\nabla_{xy}\cdot\underline{u}\,\underline{u}-\nabla_{z}\cdot\underline{w}\,\underline{u}=&-\underline{g}\nabla_{xy}\eta-\frac{1}{\rho_0}\int_z^{\eta}\underline{g}\nabla_{xy}\rho'\mathrm{d}\zeta \qquad (2.14)\\ &+\nabla_{xy}\cdot\nu_{xy}\nabla_{xy}\underline{u}+\nabla_z\cdot\nu_z\nabla_z\underline{u}-f\hat{k}\times\underline{u}+\frac{1}{\rho_0}\underline{f_u}\\ \nabla_{xy}\cdot\underline{u}+\nabla_z\cdot\underline{w}=&\,0 \qquad (2.15)\\ \frac{\partial\eta}{\partial t}+\nabla_{xy}\cdot\int_{-H}^{\eta}\underline{u}\mathrm{d}z=&\,0 \qquad (2.16)\end{aligned}$$

This amounts to assuming that the vertical scales are much smaller in magnitude than the horizontal (similar to a thin fluid approximation from lubrication theory). In other words, we assume that

$$|w|\ll|u|\sim|v| \qquad \text{and} \qquad \frac{\partial u}{\partial z}\ll\frac{\partial u}{\partial x}\sim\frac{\partial u}{\partial y} \qquad (2.17)$$

In Fig.2-1, we summarize the two sets of equations. Note that we have used the

Nonhydrostatic Equations

$$\frac{\partial \mathbf{u}}{\partial t} - (\nabla \cdot (\boldsymbol{\nu} \nabla \mathbf{u})) + \nabla p' + g \nabla_{xy} \eta = -\frac{1}{\rho_0} \int_z^\eta g \nabla_{xy} \rho' \, dz' - \nabla \cdot (\mathbf{u} \otimes \mathbf{u}) + \frac{1}{\rho_0} \mathbf{f}$$

Hydrostatic Equations

$$\frac{\partial \mathbf{u}}{\partial t} - (\nabla \cdot (\boldsymbol{\nu} \nabla \mathbf{u})) + \overbrace{0}^{p'=0} + g \nabla_{xy} \eta = -\frac{1}{\rho_0} \int_z^\eta g \nabla_{xy} \rho' \, dz' - \nabla \cdot (\mathbf{u} \otimes \mathbf{u}) + \frac{1}{\rho_0} \mathbf{f}$$

$$\frac{\partial \eta}{\partial t} + \nabla \cdot \left(\int_{-H}^{\eta} \mathbf{u} \, dz \right) = 0$$

$$\nabla \cdot \mathbf{u} = 0$$

$$\frac{\partial \rho'}{\partial t} - \nabla \cdot (\kappa \nabla \rho') = -\nabla \cdot (\mathbf{u} \rho') + f_{\rho'}$$

Figure 2-1: A summary of the non-hydrostatic ocean equations (left) and hydrostatic ocean equations (right)

equation of state to replace the transport equation for temperature and salinity with a tracer equation for the density anomaly ρ'. Henceforth, we will be working with this form of the NHS and HS equations.

2.2 Projection Method

As is common for non-hydrostatic models [35, 72, 73], we solve the NHS and HS ocean equations using a pressure-projection method [16, 101] that decouples the velocities and the pressure. These methods are based on the Helmholtz decomposition, wherein vector fields are separated into divergence-free and irrotational parts. Generally, these schemes constitute an initial step where an intermediate velocity field is computed that doesn't satisfy the divergence-free constraint and a final step where a pressure correction is used to "project out" the divergence-producing part of the velocity field. Here we will summarize the steps in the semi-implicit pressure-projection method for the non-hydrostatic and hydrostatic ocean equations as presented in [103]. The initial steps of the scheme are common to the NHS and HS equations, but the final steps are different as listed below

1. First Velocity Predictor - $\{p^{\prime,k}, \eta^k\} \rightarrow \{\underline{\bar{u}}^{k+1}, \underline{\bar{w}}^{k+1}\}$

The first predictor velocities ($\underline{\bar{u}}^{k+1}$ and $\underline{\bar{w}}^{k+1}$) are computed by solving the momentum equation using the previous time-step values for the non-hydrostatic pressure $p^{\prime,k}$ and free-surface elevation η^k

$$\frac{\underline{\bar{u}}^{k+1}}{a\Delta t} - \nabla_z \cdot \nu_z \nabla_z \underline{\bar{u}}^{k+1} + \nabla_{xy} p^{\prime,k} + g\nabla_{xy}\eta^k = \underline{F_u}^{k,k+1} \tag{2.18}$$

$$\frac{\underline{\bar{w}}^{k+1}}{a\Delta t} - \nabla_z \cdot \nu_z \nabla_z \underline{\bar{w}}^{k+1} + \nabla_z p^{\prime,k} = \underline{F_w}^{k,k+1} \tag{2.19}$$

where,

$$\begin{aligned} \underline{F_u}^{k,k+1} =& \frac{\underline{u}^k}{a\Delta t} - \frac{1}{\rho_0}\int_z^{\eta^k} g\nabla_{xy}\rho^{\prime,k}\mathrm{d}\zeta - \nabla_{xy} \cdot \underline{u}^k\,\underline{u}^k \\ & - \nabla_z \cdot \underline{w}^k\,\underline{u}^k + \nabla_{xy} \cdot \nu_{xy}\nabla_{xy}\underline{u}^k - f\hat{k} \times \underline{u}^k + \frac{1}{\rho_0}\underline{f_u}^{k,k+1} \end{aligned} \tag{2.20}$$

$$\begin{aligned} \underline{F_w}^{k,k+1} =& \frac{\underline{w}^k}{a\Delta t} - \nabla_{xy} \cdot \underline{u}^k\,\underline{w}^k - \nabla_z \cdot \underline{w}^k\,\underline{w}^k \\ & + \nabla_{xy} \cdot \nu_{xy}\nabla_{xy}\underline{w}^k + \frac{1}{\rho_0}\underline{f_w}^{k,k+1} \end{aligned} \tag{2.21}$$

with Dirichlet and Neumann boundary conditions given as,

$$\underline{\bar{u}}\Big|_{\partial\Omega_D}^{k+1} = \underline{g}_{u,D} \qquad \bar{w}\Big|_{\partial\Omega_D}^{k+1} = \underline{g}_{w,D} \qquad \frac{\partial\underline{\bar{u}}}{\partial\hat{n}}\bigg|_{\partial\Omega_N}^{k+1} = \underline{g}_{u,N} \qquad \frac{\partial\underline{\bar{w}}}{\partial\hat{n}}\bigg|_{\partial\Omega_N}^{k+1} = \underline{g}_{w,N} \tag{2.22}$$

2. Free-surface Corrector - $\underline{\bar{u}}^{k+1} \rightarrow \delta\eta^{k+1}$

The free-surface kinematic condition equation is solved using the first predictor velocities to obtain the free-surface corrector for the next timestep as

$$\frac{\delta\eta^{k+1}}{a\Delta t} - \nabla_{xy} \cdot \left[a\Delta t g(\eta^k + H)\nabla_{xy}\delta\eta^{k+1}\right] = F_\eta^{k,k+1} \tag{2.23}$$

where H is the depth of the ocean and

$$F_\eta^{k,k+1} = -\nabla_{xy} \cdot \int_{-H}^{\eta^k} \underline{\bar{u}}^{k+1} \mathrm{d}z \tag{2.24}$$

with boundary conditions ($\partial\Omega_N$ and $\partial\Omega_O$ are boundaries with wall and open conditions for the velocities, respectively)

$$\nabla_{xy}\delta\eta\big|_{\partial\Omega_N}^{k+1} \cdot \hat{n}_{xy} = \frac{1}{a\Delta t g(H+\eta^k)} \int_{-H}^{\eta^k} (\underline{\bar{u}}^{k+1} - \underline{g}_{u,D}) \cdot \hat{n}_{xy} \mathrm{dz} \tag{2.25}$$

$$\delta\eta\big|_{\partial\Omega_O}^{k+1} = g_{\eta.O} \tag{2.26}$$

3. Free-surface corrections - $\{\underline{\bar{u}}^{k+1}, \delta\eta^{k+1}\} \rightarrow \{\underline{\bar{\bar{u}}}^{k+1}, \underline{\bar{\bar{w}}}^{k+1}, \eta^{k+1}\}$

The free-surface corrector and first velocity predictors are then used to algebraically compute the second predictor velocities and the free-surface elevation for the next timestep as

$$\underline{\bar{\bar{u}}}^{k+1} = \underline{\bar{u}}^{k+1} - a\Delta t g \nabla_{xy} \delta\eta^{k+1} \qquad \eta^{k+1} = \eta^k + \delta\eta^{k+1} \tag{2.27}$$

Once the second predictor velocities and the new free-surface elevations are computed, the steps followed to arrive at the final velocities differ for the NHS and HS equations.

NHS equations:

4. Pressure Corrector - $\bar{\bar{\boldsymbol{u}}}^{k+1} \rightarrow \delta p'^{,k+1}$

The non-hydrostatic pressure correction is computed using the second predictor velocities by solving the following pressure-Poisson equation (PPE).

$$\nabla_{xy}^2 \delta p'^{,k+1} + \nabla_z^2 \delta p'^{,k+1} = \frac{\nabla_{xy} \cdot \underline{\bar{\bar{u}}}^{k+1}}{a\Delta t} + \frac{\nabla_z \cdot \underline{\bar{\bar{w}}}^{k+1}}{a\Delta t} \tag{2.28}$$

with boundary conditions ($\partial\Omega_{NS,S}$, $\partial\Omega_\eta$ and $\partial\Omega_O$ are boundaries with no-slip, slip,free-surface and open boundary conditions for the velocities)

$$\nabla \delta p'\big|_{\partial\Omega_{NS,S}}^{k+1} \cdot \hat{n} = \frac{1}{a\Delta t}(\bar{\bar{\underline{u}}}^{k+1} - \underline{g}_{u,D}) \cdot \hat{n}_{xy} + \frac{1}{a\Delta t}(\bar{\bar{\underline{w}}}^{k+1} - \underline{g}_{w,D}) \cdot \hat{n}_z \tag{2.29}$$

$$\nabla \delta p'\big|_{\partial\Omega_\eta}^{k+1} = 0 \tag{2.30}$$

$$\nabla \delta p'\big|_{\partial\Omega_O}^{k+1} = g_{O_{p'}} \tag{2.31}$$

5. Final Velocity and Pressure - $\{\bar{\bar{\boldsymbol{u}}}^{k+1}, \delta p'^{,k+1}\} \rightarrow \{p'^{,k+1}, \boldsymbol{u}^{k+1}\}$

The final divergence-free velocities and non-hydrostatic pressure are computed using the pressure corrector as

$$\underline{u}^{k+1} = \bar{\bar{\underline{u}}}^{k+1} - a\Delta t \nabla_{xy} \delta p'^{,k+1} \tag{2.32}$$

$$\underline{w}^{k+1} = \bar{\bar{\underline{w}}}^{k+1} - a\Delta t \nabla_z \delta p'^{,k+1} \tag{2.33}$$

$$p'^{,k+1} = p'^{,k} + \delta p'^{,k+1} \tag{2.34}$$

HS equations:

4. Final Velocity - $\bar{\bar{\underline{u}}}^{k+1} \rightarrow \underline{w}^{k+1}$

The second predictor horizontal velocities become the final horizontal velocities ($\underline{u}^{k+1} = \bar{\bar{\underline{u}}}^{k+1}$) and the final vertical velocities are reconstructed from the 3D continuity equation such that the divergence-free constraint is satisfied.

$$\nabla_z \cdot \underline{w}^{k+1} = -\nabla_{xy} \cdot \underline{u}^{k+1} \tag{2.35}$$

with boundary condition

$$\underline{w}^{k+1}\big|_{-H} = -\underline{u}^{k+1} \cdot \nabla_{xy} H \tag{2.36}$$

2.3 Hybridizable Discontinuous Galerkin Method

Finite element methods offer high-order solutions and ease of implementation on unstructured grids which makes them suitable candidates for modelling flows in complex domains. In particular, the Discontinuous Galerkin (DG) finite element methods are very attractive for modelling advection-dominated flows as the discontinuous polynomial spaces can capture steep gradients and wave behaviour leading to stable and flexible schemes in comparison to the standard Continuous Galerkin (CG) finite element methods. It is also known that DG-FEM methods are well-suited for adaptive mesh refinement techniques which could be critical in alleviating the computational demand for large-scale ocean modelling.

Hybridizable discontinuous Galerkin (HDG) finite element methods were introduced in [19] for second-order elliptic problems to address one of the key drawbacks of DG methods which is the spatial duplication of degrees of freedom. HDG schemes allow for discontinuous solutions while solving globally coupled unknowns that only have support on the element interfaces. This results in a significantly reduced linear system to be solved and a comparison of the distribution of degrees of freedom for the CG-FEM, DG-FEM and HDG-FEM is shown in Fig.2-2. Since its invention, HDG has been applied to a wide variety of problems including linear and nonlinear convection-diffusion [78, 77], linear elasticity [99], Maxwell's equations [80, 2, 67], incompressible flows [18, 79] and compressible flows [85, 84, 76]. More recently, an HDG scheme for the incompressible Navier-Stokes with Boussinesq approximation based on projection method [16, 101] was proposed in [106, 102, 103, 107] with implementation refinements in [30, 33].

In HDG schemes, the element-local solutions are parameterized in terms of a numerical trace that lives on the global edge space. Then, a glocal problem is solved on this edge space by enforcing normal flux continuity and the computed values of the numerical trace are used to reconstruct the element-local solutions. Note that once the numerical trace is computed on the global edge space, the element-local solutions can be reconstructed in an independent and parallel fashion suitable for modern-day

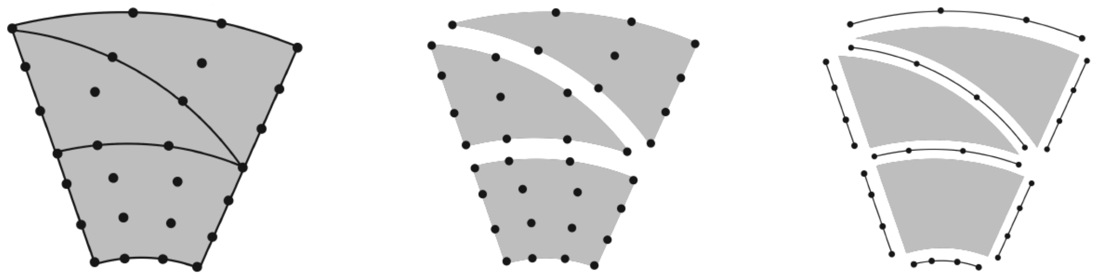

Figure 2-2: Schematic illustrating the coupled degrees of freedom for CG-FEM (left), DG-FEM (middle) and HDG-FEM (right) - taken from [31]

computer architecture. Furthermore, these schemes also allow for local, element-by-element postprocessing options to obtain new approximations by exploiting the superconvergence properties of the HDG [77] method.

Chapter 3

Multidynamics Model

Non-hydrostatic models are required to capture phenomena such as nonlinear internal waves, subduction, convection plumes and overturning which are believed to be crucial to the energy transfer between the slow-moving large-scale motions and the high-speed mixing scales in the ocean [34]. However, it is well-understood in the literature that relaxing the hydrostatic pressure constraint comes at a significant computational cost. The three-dimensional globally-coupled elliptic equation that needs to be solved for the non-hydrostatic pressure component (as shown in Section 2.2) accounts for the bulk of the workload in most NHS solvers [35, 73, 111]. This three-dimensional pressure-Poisson equation is poorly conditioned due to the fact that the vertical and horizontal second-derivative terms are typically two orders of magnitudes apart. Therefore, over the last few decades, research has been directed towards making NHS simulations more feasible. In this chapter, we briefly discuss works from the literature that address this issue and then present our proposed multi-dynamics model.

There have been many efforts made towards improving the efficiency of NHS models over the years. In [91], a non-hydrostatic finite-volume algorithm similar to the MIT GCM [72] is developed in the Julia programming language that solves geophysical flows on CPUs and GPUs. In [7], a three-mode time-split algorithm is developed for non-hydrostatic processes in free-surface ocean models. A semi-implicit and variable layers (SIVL) scheme for the non-hydrostatic pressure component calculation was introduced in [100] as a method to improve solver efficiency. The PSOM model [70] uses a multigrid method to solve for the non-hydrostatic pressure component in a finite-volume framework.

Although most existing ocean solvers are low-order finite volume codes, there are a few high-order solvers including SEOM [74], the DG NHS code presented in [83, 82], and our MSEAS non-hydrostatic HDG ocean model [106, 33]. Such high-order methods are often able to produce more accurate solutions than low-order methods for similar computational costs [44, 104]. In [30], a distributed implementation of the HDG projection method algorithm is developed in the context of large-scale ocean simulations to make the computational cost more tractable. Adaptive mesh refinement schemes [32, 95, 88], which allow for resolution wherever necessary in the domain, have also been investigated as a means to alleviate the computational demand of NHS models.

Another approach for reducing the computational cost of these simulations is to use approximate NHS models. In [73], the authors propose a quasi-hydrostatic model wherein the precise balance between gravity and the forces due to the pressure gradient is relaxed by treating the Coriolis force exactly. However, this model does not account for an NHS pressure component and consequentially, the forces due to its gradient. A non-hydrostatic model with an isopycnal (density-following) coordinate system was proposed in [111] and it was demonstrated that this model is able to capture nonlinear internal solitary waves for some idealized ocean test cases. Yet, this model has a significant limitation in that its unable to represent unstable stratification and overturning effects that are commonly associated with non-hydrostatic phenomena.

3.1 Multi-Dynamics Model

The computational cost of non-hydrostatic models aside, a big reason why the majority of ocean models and solvers are based on the hydrostatic approximation is that these solvers can capture many oceanic processes very accurately. The hydrostatic

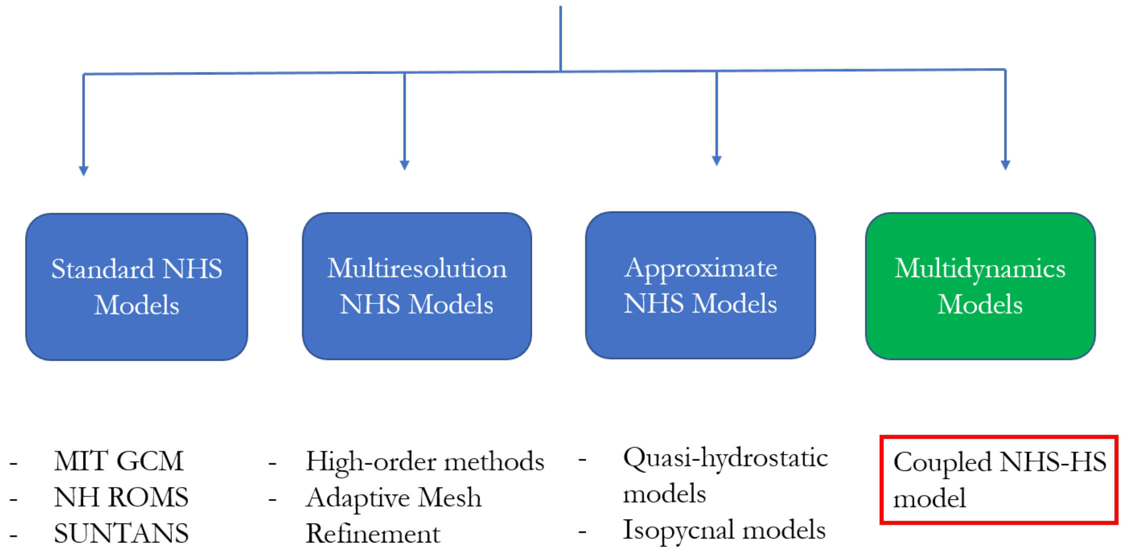

Figure 3-1: Different approaches to deal with the high computational cost associated with non-hydrostatic simulations

primitive equations (HPE) are capable of capturing the global circulation of oceans, wind-driven gyres, geostrophic eddies, and many such features that exhibit horizontal length scales much larger than the vertical ones. The hydrostatic approximation breaks down when the horizontal length scales of the phenomena in consideration become comparable to the vertical length scales [73]. Therefore, non-hydrostatic effects tend to be localized and this forms our motivation for developing a coupled NHS-HS model capable of treating different regions of a domain to be non-hydrostatic and hydrostatic by solving the appropriate equations with the appropriate solvers at the appropriate physical locations and times.

Since we have developed solvers for both the non-hydrostatic and hydrostatic ocean equations (as described in 2.1), we could imagine splitting our domain into subdomains and employing the requisite solver for each subdomain. However, it is not obvious how the subdomains would be coupled, and devising an efficient strategy to facilitate optimal communication between the NHS and HS subdomains is crucial to this coupled modeling scheme. Our numerical research questions include: What are the dynamical regimes and domain properties for which multi-dynamics (NHS and HS) solvers would be most efficient? Can HDG numerical schemes be developed such that different dynamics occur within the same solver? Are there advantages for HDG to achieve this multi-dynamics capability? How could the NHS and HS domains be connected efficiently and accurately? How could the NHS and HS cell types be modified during the simulation? One could add several other related questions to this list. In what follows, we will address several of them.

3.1.1 Preliminary subdomain coupling ideas

One possible approach could be to employ an upwind-Dirichlet coupling between the NHS and HS subdomains. In the degenerate case of just two subdomains in our full computational domain, we would solve the "upwind" subdomain with an open boundary condition at the boundary that coincides with the other subdomain and supply the computed values at the boundary to the "downstream" subdomain through a Dirichlet boundary condition (as shown in Fig.3-2). However, this method is unlikely to be robust for a few reasons. Barring the simple advection-dominated problems, it would be difficult to identify the upstream subdomains. Additionally, this method would almost entirely decouple the state variables in the different subdomains.

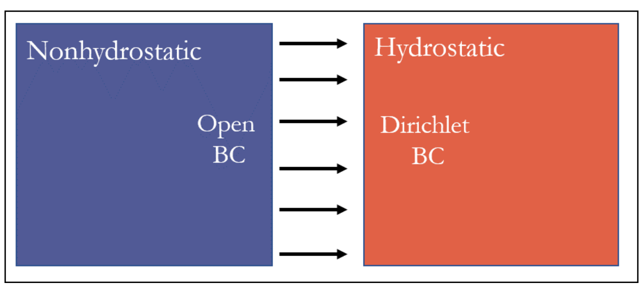

Figure 3-2: Schematic of an upwind Dirichlet approach to coupling the nonhydrostatic and hydrostatic subdomains

Another possible approach would be to employ a Schwarz method [36, 98] to couple the different subdomains. Here, we would define our subdomains such that they include overlapping regions and then solve each subdomain completely independently (as shown in Fig.3-3). Following this, we would perform iterations within each timestep wherein we re-solve the problem on each subdomain with boundary conditions obtained from the solutions in the neighbouring subdomains until convergence is attained. Although this method might facilitate better communication between subdomains, it introduces a possibility of convergence issues and an increased computational cost associated with the extended domains and iterations within each timestep.

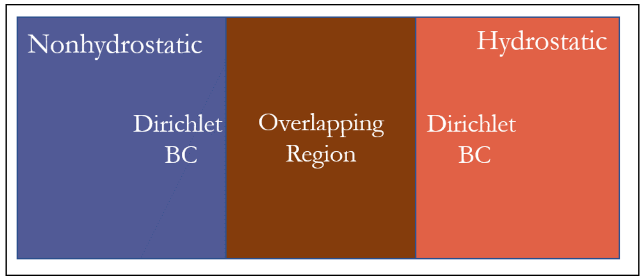

Figure 3-3: Schematic of a domain decomposition approach to coupling the non-hydrostatic and hydrostatic subdomains

3.1.2 Novel Projection method-based coupling of multi-dynamics subdomains

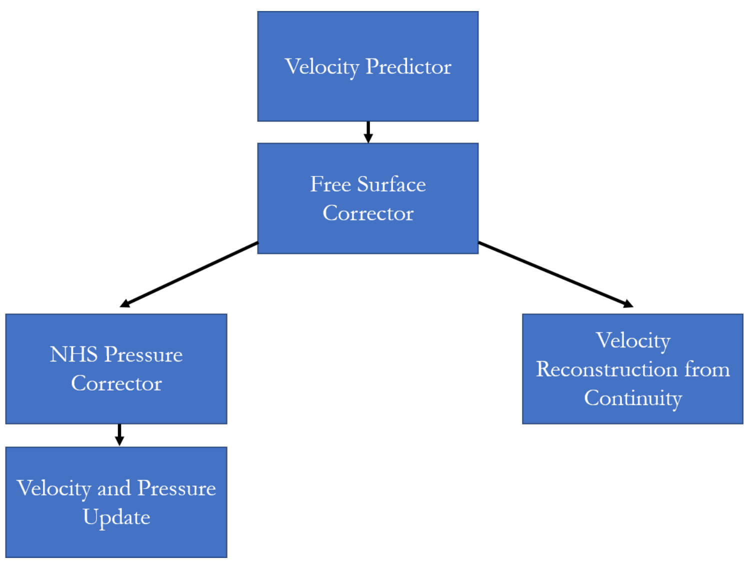

Figure 3-4: Summary of projection method steps involved in solving the non-hydrostatic (left) and hydrostatic (right) ocean equations

Figure 3-4 summarizes the steps involved in the HDG pressure-projection method for the non-hydrostatic and hydrostatic ocean equations. Recognizing that the solution process for the two models only differs in the latter steps, we devise a new algorithm wherein the initial projection method steps are executed on the entire domain in a coupled manner, and then, the appropriate final steps are carried out on the NHS and HS subdomains. This way, we solve smaller, local pressure-Poisson equations for the non-hydrostatic pressure in the NHS subdomains, thereby making computational savings.

We describe a simple example to illustrate this algorithm. Consider a rectangular domain where we expect the flow to be hydrostatic towards the right and non-hydrostatic towards the left, as shown in Fig.3-5. The domain is split into two at $x = x_{split}$ and the left subdomain is labelled to be NHS and the right to be HS. At each timestep, the intermediate values from the projection method are transferred to the respective subdomains where the dynamic-appropriate steps are followed to compute the final velocities and pressure. The computed solutions are then returned to the full domain for the next timestep.

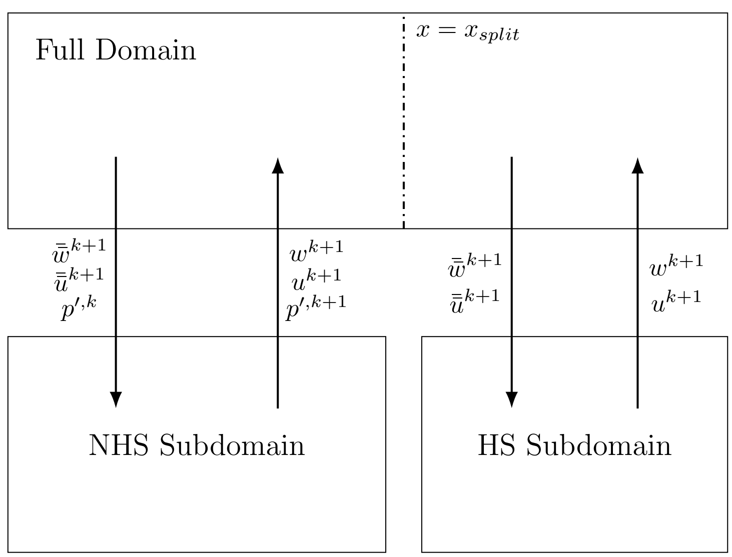

Figure 3-5: Schematic illustrating a split domain with an NHS subdomain on the left and an HS subdomain on the right. The intermediate solutions are transferred to the subdomains where the appropriate equations are solved and the final velocities and pressure are returned to the full domain.

Overall, at each time step, we execute the steps listed in Algorithm 1.

Algorithm 1 Projection method-based coupling algorithm

Compute first velocity predictors $(\underline{\bar{u}}^{k+1}, \underline{\bar{w}}^{k+1})$ in the full domain
Compute free-surface corrector $\delta\eta^{k+1}$ in the full domain
Compute second velocity predictors $(\underline{\bar{\bar{u}}}^{k+1}, \underline{\bar{\bar{w}}}^{k+1})$ and free-surface elevation η^{k+1}
Then, for each subdomain
if NHS subdomain **then**
    Transfer $(\underline{\bar{\bar{u}}}^{k+1}, \underline{\bar{\bar{w}}}^{k+1})$ and $p'^{,k}$ to subdomain
    Solve local pressure-Poisson equation to compute $p'^{,k+1}$ and $(\underline{u}^{k+1}, \underline{w}^{k+1})$.
    Transfer $\underline{u}^{k+1}$, $\underline{w}^{k+1}$ and $p'^{,k+1}$ to the full domain
else
    Set non-hydrostatic pressure to zero - $p'^{,k+1} = 0$
    Set final horizontal velocities as $\underline{u}^{k+1} = \underline{\bar{\bar{u}}}^{k+1}$
    Reconstruct final vertical velocities $\underline{w}^{k+1}$ from the continuity equation
    Transfer $\underline{u}^{k+1}$, $\underline{w}^{k+1}$ and $p'^{,k+1}$ to the full domain
end if

It is important to note that to solve the local pressure-Poisson problems in the NHS subdomains, we need to specify boundary conditions for $\delta p'$ along the newly formed internal boundaries. We can choose from a few reasonable options here and it is not obvious which would be the optimal choice. The possible choices include,

1. Homogeneous Dirichlet boundary condition - $\delta p'^{,k+1} = 0$

   This would be an appropriate boundary condition if the internal boundary is well within a hydrostatic region of the domain

2. Imposing the previous timestep data - $\delta p'^{,k+1} = \delta p'^{,k}$

   This amounts to assuming that the divergence of the velocity predictor has not changed $\nabla \cdot \bar{\bar{\boldsymbol{u}}}^{k+1} \approx \nabla \cdot \bar{\bar{\boldsymbol{u}}}^{k}$, and therefore would be valid if the flow near the boundary is almost steady.

3. Homogeneous Neumann boundary condition - $\partial \delta p'^{,k+1} / \partial n = 0$

   This boundary condition allows for a larger degree of freedom for the values $\delta p'$ and could be used when we have little information about the flow near the boundary (similar to open boundary conditions).

We note that these boundary conditions might reduce to the same boundary condition when considering a problem with static subdomains and hydrostatic initial conditions.

3.2 New numerical non-hydrostatic parameters

Non-hydrostatic effects, such as nonlinear internal waves, are often localized and associated with small horizontal length scales [110, 10]. The accuracy of models representing many other localized ocean wave effects would benefit from some local non-hydrostatic treatment [47, 46, 27, 28, 50, 51], at least for including wave-breaking effects. Therefore, it would be useful to have a method to identify regions of our domain exhibiting NHS behaviour so that the NHS solvers can be employed appropriately locally in space and time, where and when needed.

The hydrostatic approximation can be thought of as a thin-fluid assumption and we can expect to require that

$$w \ll u \qquad \text{and} \qquad h \ll L \qquad \text{and} \qquad \frac{\partial u}{\partial z} \ll \frac{\partial u}{\partial x} \tag{3.1}$$

where L and h are the horizontal and vertical length scales of the motions, and u and w are the horizontal and vertical velocities. In [73], the authors present the following non-dimensional non-hydrostatic parameter to quantify NHS behaviour

$$n = \frac{u^2}{L^2 N^2} = \frac{\gamma^2}{R_i} \ll 1 \implies \text{Hydrostatic} \tag{3.2}$$

where $N^2 = -(g/\rho_0)(\partial\rho/\partial z)$ is the Brunt-Väisälä frequency, $\gamma = h/L$ is the aspect ratio and $R_i = N^2 h^2/u^2$ is the Richardson number. This parameter accounts for the fact that the hydrostatic approximation would be valid even for small aspect-ratio problems if the stratification is strong enough ($R_i >> 1$).

Looking at the pressure-Poisson equation (from Sec.2.2) that determines the NHS pressure field, we see that the forcing function is a scaled divergence of the first velocity predictors

$$\nabla^2_{xy}\delta p^{\prime,k+1} + \nabla^2_z \delta p^{\prime,k+1} = \frac{\nabla_{xy} \cdot \underline{\bar{\bar{u}}}^{k+1}}{a\Delta t} + \frac{\nabla_z \cdot \underline{\bar{\bar{w}}}^{k+1}}{a\Delta t} \tag{3.3}$$

Further, we know that the Green's function of the Laplace operator rapidly decays and we can thereby expect a correlation between domain regions with non-zero values of forcing and non-zero values of NHS pressure corrector. Therefore, we construct a new numerical non-hydrostatic parameter as

$$\alpha = \frac{\nabla_{xy} \cdot \underline{\bar{\bar{u}}}^{k+1}}{a\Delta t} + \frac{\nabla_{z} \cdot \underline{\bar{\bar{w}}}^{k+1}}{a\Delta t} \tag{3.4}$$

and expect it can track regions of non-zero pressure corrector values $\delta p'$.

This new parameter could be used to devise an adaptive multi-dynamics algorithm where the subdomains are evolved dynamically over time. Moreover, since we solve for both the state variables and the derivatives in the HDG framework, we can readily compute this numerical non-hydrostatic parameter.

Chapter 4

Numerical Investigation

In this chapter, we verify some of the claims made in the literature about the computational bottleneck of NHS models and then present various results from a 2D first-implementation of the proposed multi-dynamics model. Firstly, we introduce an idealized problem that will serve as the test case for all the following numerical experiments. Our in-house, parallelized, non-hydrostatic C++ HDG code [33] is profiled to demonstrate that the pressure-Poisson equation solved for the NHS pressure component is indeed the computational bottleneck. Following this, we present qualitative validation of the C++ HDG code against another finite-volume NHS solver. The multi-dynamics model is implemented and compared with standard NHS simulations to realize computational savings and evaluate accuracy. Finally, we look at an NHS parameter that can serve as a tool to predict non-hydrostatic behaviour and facilitate extension to an adaptive multi-dynamics model.

4.1 Rayleigh-Taylor Instability-Driven Striations

Gravity-driven instabilities seen at interfaces between fluids of different densities are referred to as Rayleigh-Taylor (RT) instabilities. These instabilities are observed in processes that span a wide range of length scales ranging from supernova explosions [92] to turbulence mixing [8, 112]. RT instabilities have garnered a lot of attention over the years and there have been many investigations into the linear stability analysis

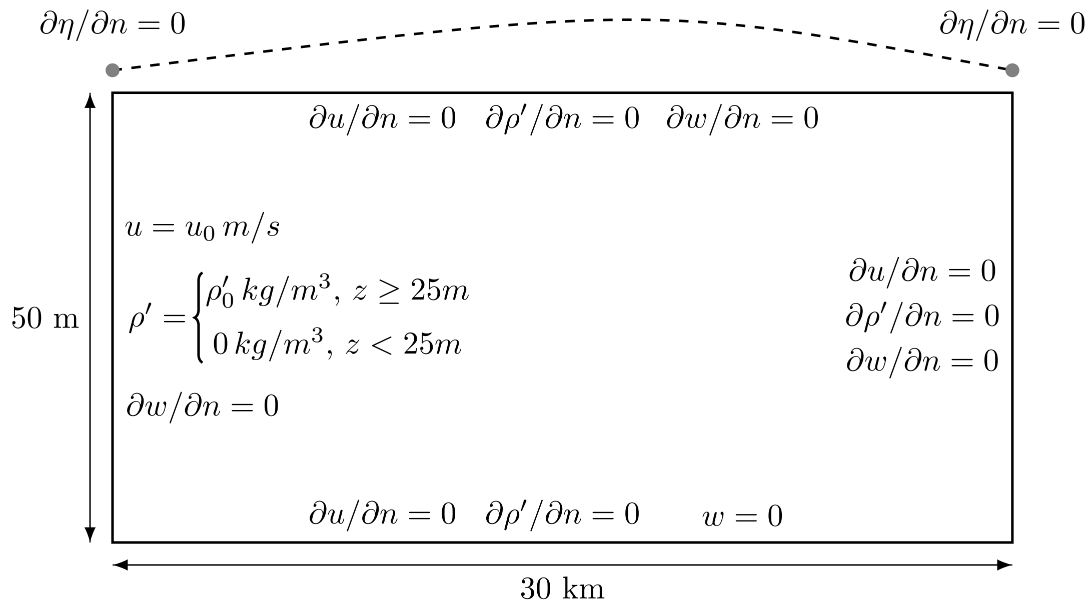

Figure 4-1: Schematic of the domain and boundary conditions considered for the Rayleigh-Taylor instability-driven striations test case. Here, u_0 denotes the background velocity, and ρ'_0 denotes the difference in density between the initial domain density and the density of the cooler water being dragged into the domain. The vertical momentum diffusivity is chosen to be $0.008\, m/s^2$ and the vertical tracer diffusivity is set to $0.004\, m/s^2$ while the horizontal momentum and tracer diffusivities are set to $100\, m/s^2$

[53, 113], nonlinear [25] stability analysis and RT instabilities in the context of ocean dynamics [22, 109, 21, 81].

We have also observed several hydrostatic traces of such instabilities in several of our MSEAS [75] PE simulations [40, 42, 1].

We construct an idealized test case featuring Rayleigh-Taylor instability-driven striations which we will use for all the following numerical experiments. We consider a two-dimensional domain of depth 50 metres and length 30 kilometres with a constant background velocity u_0. We model colder water being pulled into the domain through the left boundary by imposing an appropriate density distribution at the left boundary. Figure 4-1 illustrates the parameters used to model this problem along with the relevant boundary conditions and dimensions. As the denser water is advected into the domain, the opposing buoyancy and gravitational forces interact

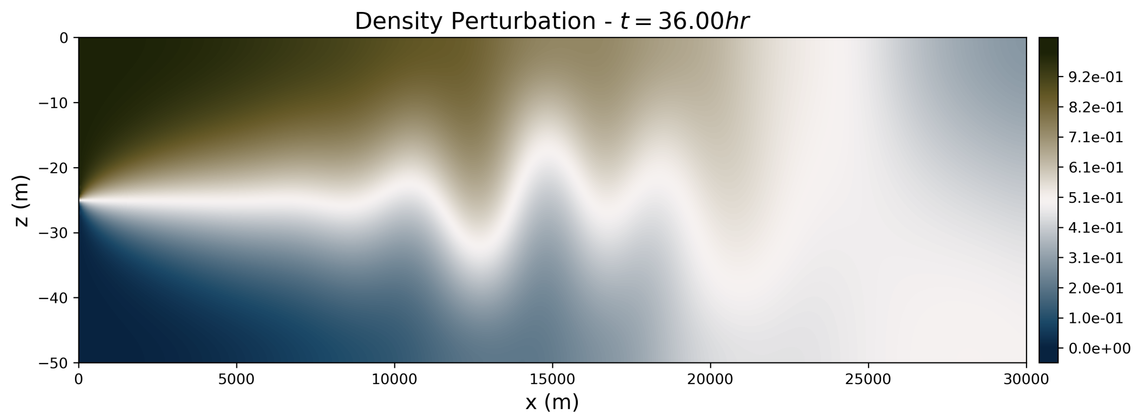

Figure 4-2: Density perturbation ρ' profile at $t = 36\,hr$ illustrating the Rayleigh-Taylor instability-driven striations that develop as the denser water is pulled into the domain. These plots correspond to a background velocity of $u_0 = 0.3\,m/s$ and a density perturbation of $\rho'_0 = 1\,kg/m^3$.

with each other leading to Rayleigh-Taylor instability-driven striations as shown in Fig.4-2.

4.2 Validation with NHS Finite Volume Code

Before we begin our numerical investigations, we verify the HDG non-hydrostatic solver against our benchmarked in-house finite-volume method (FVM) solver [105, 62]. The FVM solver has non-hydrostatic capabilities but unlike the HDG solver, it does not accommodate a free-surface (rigid-lid approximation). We simulate the RTI problem described in the previous section using the two solvers on a 200×10 grid with a polynomial order of $p = 3$ and compare the solutions.

Figure 4-3 compares the velocities and density perturbation produced by the HDG and finite-volume codes at $t = \{12\,hr, 24\,hr\}$. We see that the two solutions show good agreement at $t = 12\,hr$ in terms of the time scales of the flow and magnitudes of each state variable. However, at $t = 24\,hr$, although the primary features of the flow look similar, we see that the HDG solution shows density perturbation waves being formed that aren't captured by the finite-volume code and this can be attributed to the different free-surface models used by the two solvers. We repeat this experiment while imposing a wind shear of $\partial u/\partial y = 5\,dyn/cm^2$ along the top boundary and see that once again, the two sovlers produce qualitatively similar solutions as shown in Fig.4-4.

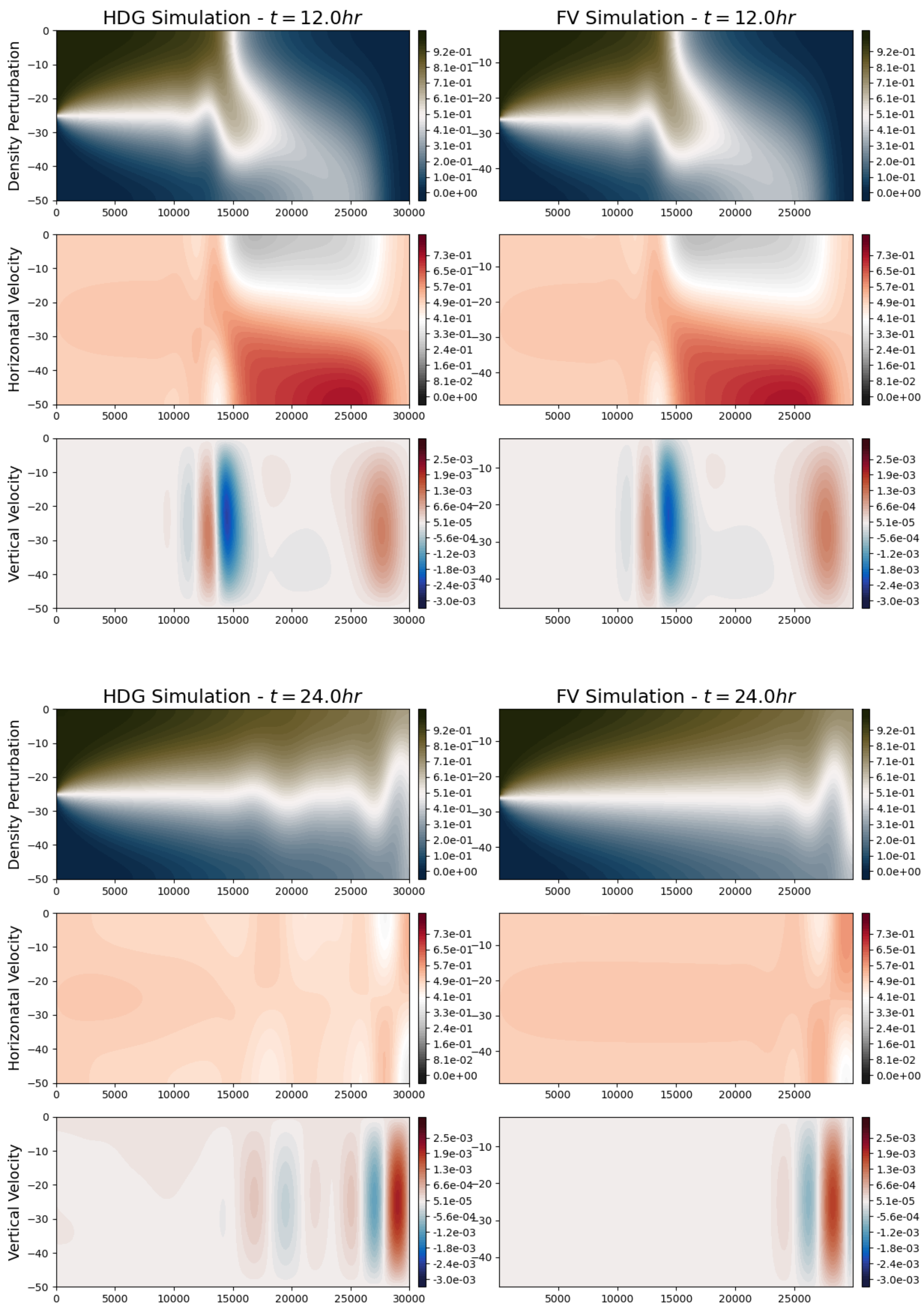

Figure 4-3: Comparison of the density perturbation and velocities between the FVM and HDG solutions to the RTI test case without wind forcing at $t = \{12\,hr, 24\,hr\}$

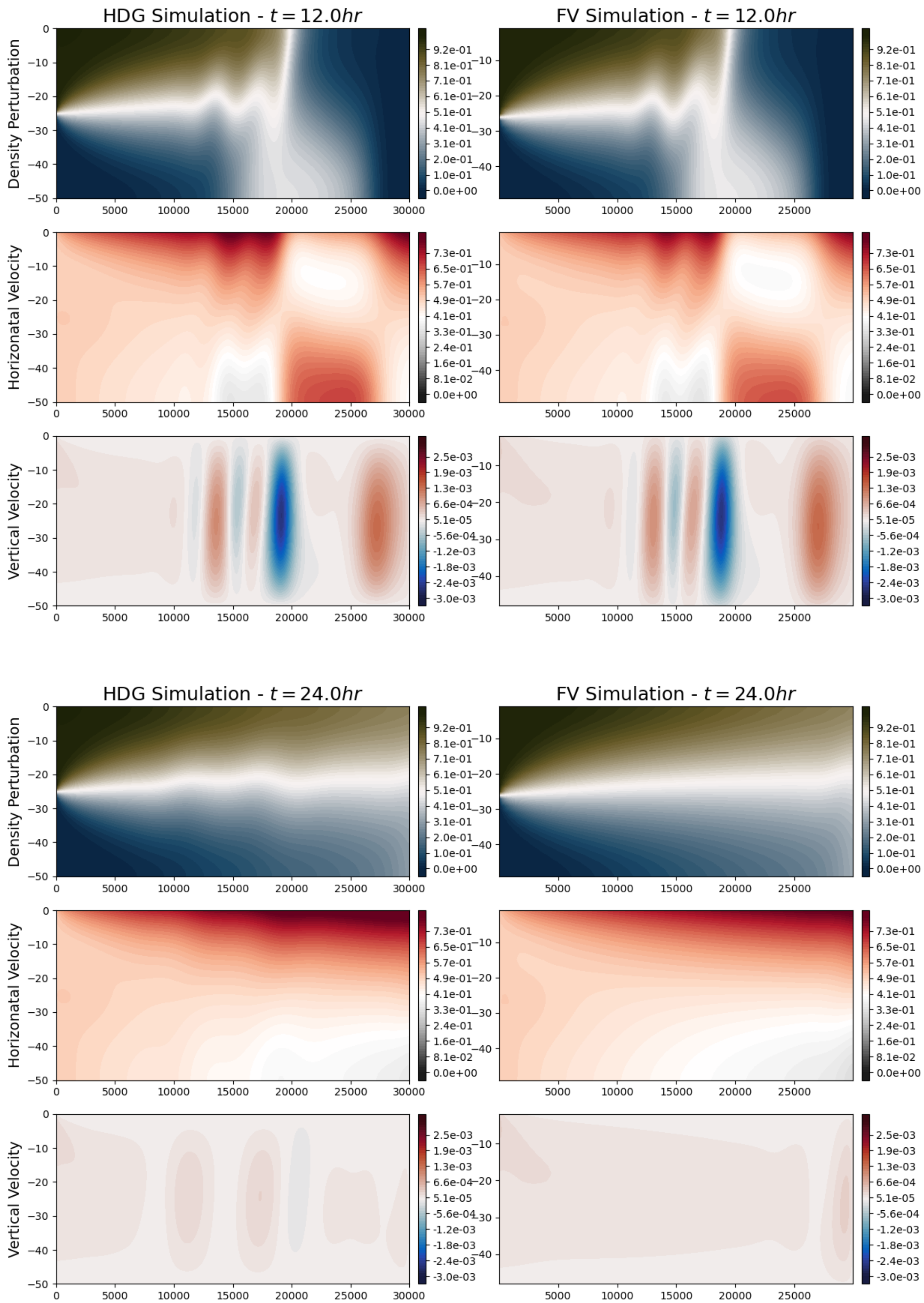

Figure 4-4: Comparison of the density perturbation and velocities between the FVM and HDG solutions to the RTI test case with wind forcing at $t = \{12\,hr, 24\,hr\}$

4.3 Code Profiling Results

In order to understand the performance and computational bottlenecks within our C++ HDG ocean solver, we perform a series of timing analyses, and the results are presented in this section. As described in Section 2.2, for each timestep of a non-hydrostatic simulation, the code assembles and solves four systems of equations as shown below in Algorithm 2.

Algorithm 2 Equations solved in the projection method at each timestep

1: Solve momentum equations to compute first velocity predictors
2: Solve free-surface evolution equation to compute the free-surface corrector
3: Solve the pressure-Poisson equation to compute the NHS pressure component
4: Solve the tracer evolution equation to compute the density perturbation

Figure 4-5 shows the statistics generated from a timing analysis for a simulation of our RTI-induced striations test case ($u_0 = 0.5\, m/s$ and $\rho'_0 = 1\, kg/m^3$). We see that for various choices of grid resolution and solutions orders, computing the solution to the pressure-Poisson equation (PPE) accounts for about 50% of the total compute time. The globally coupled nature of elliptic PDEs makes them expensive to solve. Furthermore, for field-scale ocean applications, the PPE is poorly conditioned because the vertical second derivative terms are up to two orders of magnitude larger than the horizontal second derivative terms [35, 73]. The timing analyses also show that an increase in vertical resolution further increases the fraction of computational cost spent on the pressure corrector step (Fig.4-6 (left)). We also see that for lower-order solutions, the pressure corrector step can account for up to 70% of the total computational workload (Fig.4-6 (right)).

Table 4.1 summarizes the condition number of each linear system and the number of iterations required by different iterative schemes to solve the system. The condition number of the PPE linear system and the iteration requirement is about two orders of magnitude greater than that of the other linear systems. We also see that the conjugate gradient solver proves to be the most efficient and this is consistent with what we expect given that the linear system arising from the HDG discretization is symmetric positive definite (SPD).

	Condition Number	Iteration Count		
		CG	BiCGStab	GMRES
Velocity Predictor	20	50	40	50
Free-surface Corrector	100	100	50	100
Pressure Corrector	40000	1000	900	10000
Tracer Evolution	30	50	40	50
Total Wall Clock Time		6.1s	9.1s	43.2s

Table 4.1: Summary of condition number and iteration count with different solvers for each projection method step. The pressure corrector system is poorly conditioned and requires far more iterations until convergence than the other systems. The conjugate gradient solver performs best in terms of wall-clock time.

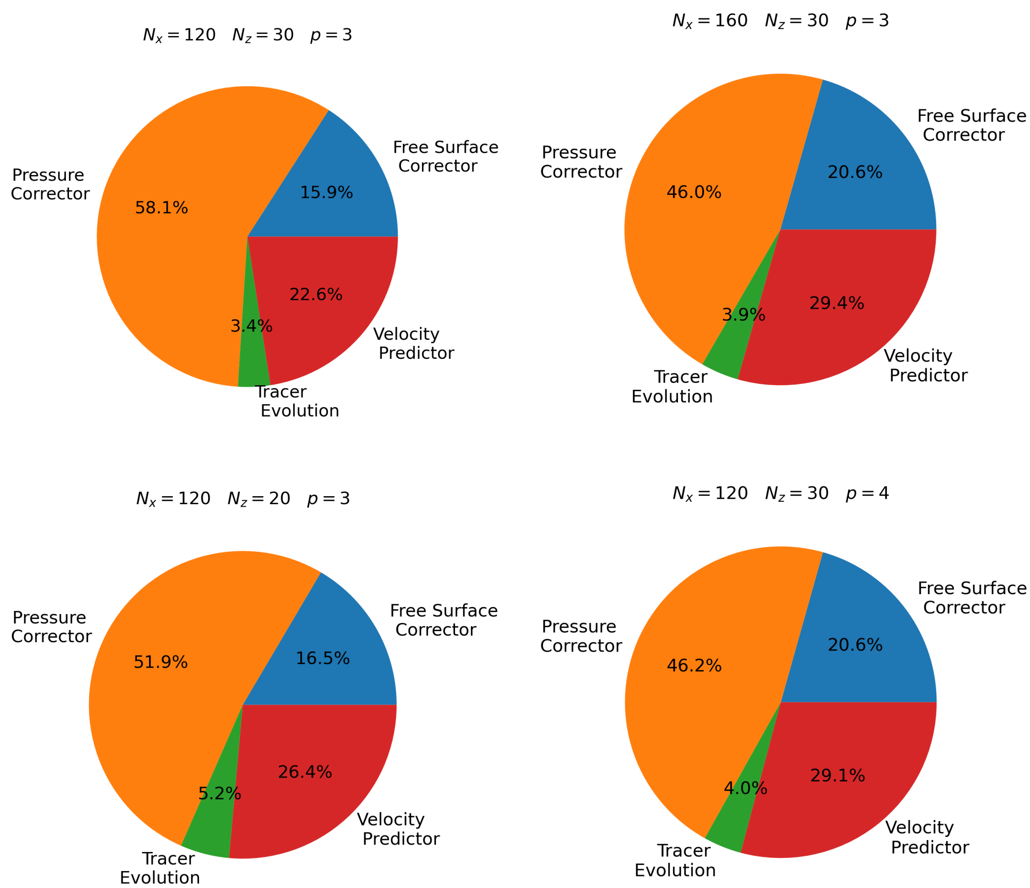

Figure 4-5: Distribution of computational cost associated with the different solutions steps involved within each timestep of a non-hydrostatic simulation. We see that the pressure corrector step accounts for about 50% of the computational budget across various resolutions and solution orders. The timing analyses are conducted on simulations of the RTI-induced striations test case.

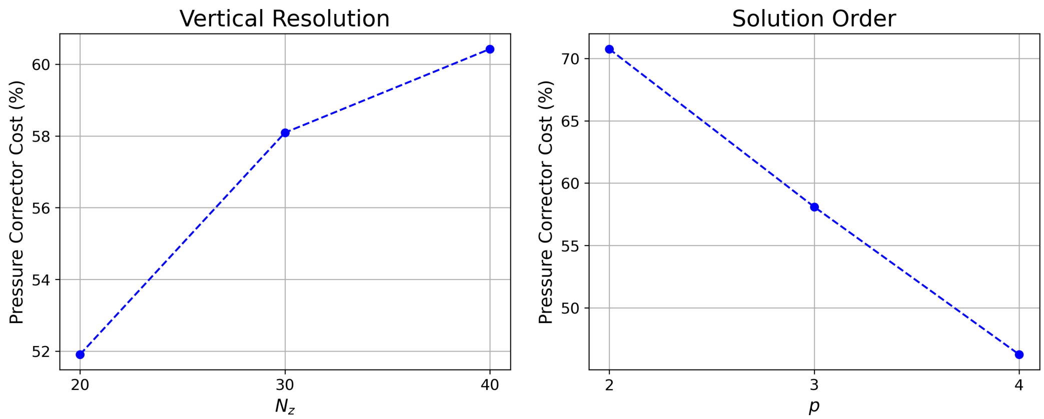

Figure 4-6: The fraction of the total computational budget consumed by the pressure corrector step as a function of vertical resolution and solution order. The timing analyses are conducted on simulations of the RTI-induced striations test case.

4.4 Split Domain Results

We have defined our test problem and empirically demonstrated that the pressure-Poisson equation for the NHS pressure is our solver's computational bottleneck. Now, we implement our multi-dynamics model on a simple test case and evaluate the model's accuracy and computational savings. For the following simulations, we consider the density difference between the initial domain density and the incoming water from the left boundary to be $\rho'_0 = 2\,kg/m^3$. This increased density anomaly causes the flow to quickly re-stratify such that the regions towards the outflow boundary of the domain are almost hydrostatic. We then consider a split-domain setup where the domain is divided into two subdomains at $x_{split} = 3L/4 = 22.5\,km$. A homogeneous boundary condition for the NHS pressure corrector ($\delta p' = 0$) is imposed along the subdomain dividing boundary for each of the following simulations. Note that the errors in the following analyses are calculated and compared in the L_2-norm as

$$L_2\,Error\,(u_{ref}, u) = \sqrt{\frac{\sum_{K\in\mathcal{T}_h}\int_K \|u_{ref} - u\|^2 \mathrm{d}K}{\sum_{K\in\mathcal{T}_h}\int_K \|u_{ref}\|^2 \mathrm{d}K}} \tag{4.1}$$

Case 1: NHS-NHS Split Domain

For our first investigation, we employ a split-domain solver comprising of NHS solvers for both subdomains and compare the resulting solution to the standard NHS solution. In this case, the only error we have introduced in the split-domain model is due to the homogeneous boundary condition we impose along $x = x_{split}$ for the NHS pressure corrector. Therefore, we expect the error in the split-domain solution compared to the standard NHS solution to be minimal.

Figure 4-7 and 4-8 show the density perturbation and NHS pressure profiles at $t = 12\,hr$ and $t = 24\,hr$, respectively. As expected, throughout the simulation, we see that the relative error is below 0.01% for the density perturbation and below 1% for the NHS pressure. The errors in velocity were also computed and they were limited to 0.1% for the horizontal velocity and to 0.1% for the vertical velocities. Looking at the absolute error plots, we see that the errors seem to be mostly localized to $x_{split} < x < L$. We also note that the jump in error around timestep number 300 indicates the advection flow reaching the subdomain dividing boundary and that the oscillatory nature of the NHS pressure error curves is due to its wave train-like profile as seen in Fig.4-8.

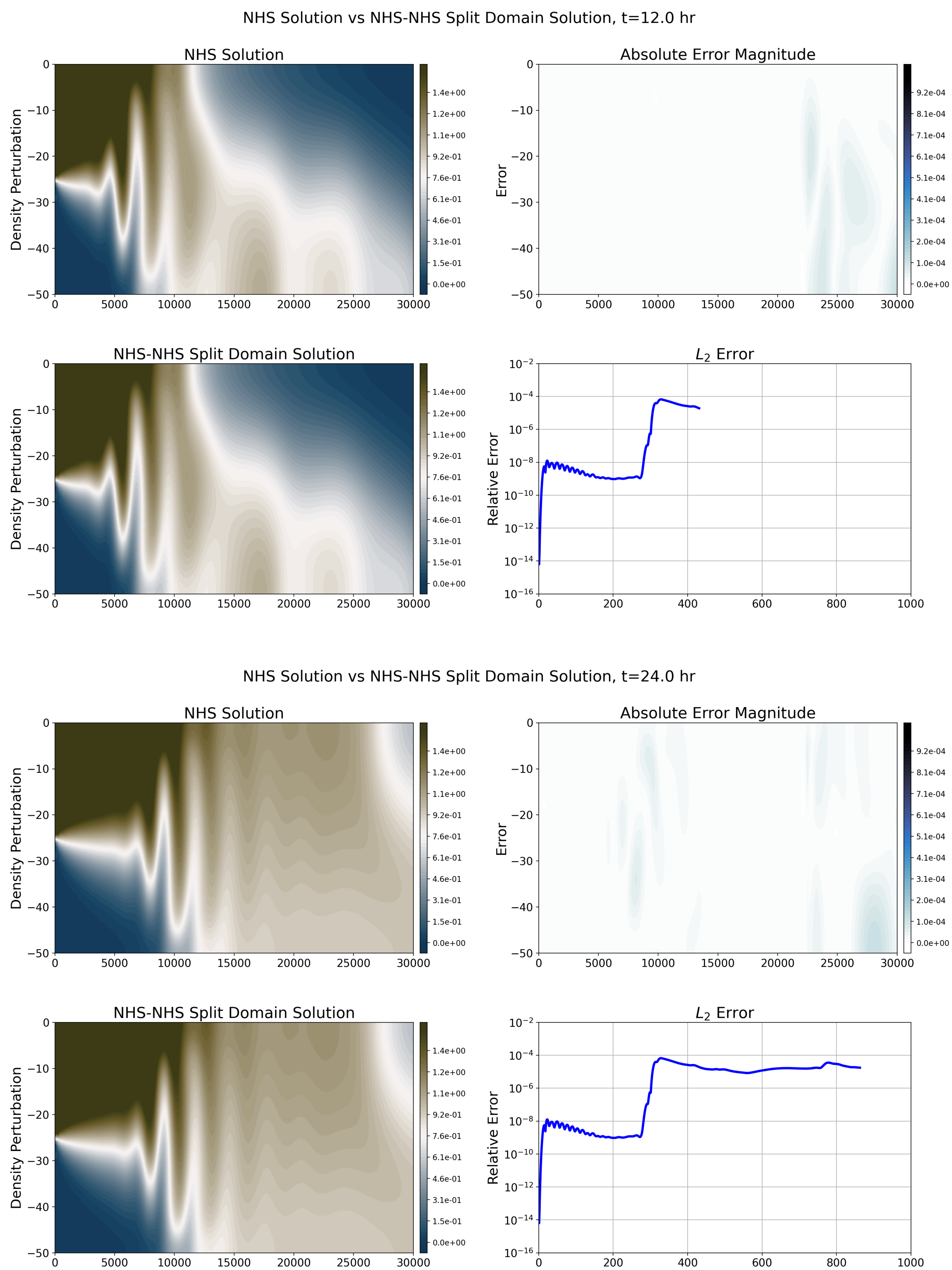

Figure 4-7: Comparison of the density perturbation between a split-domain NHS-NHS solver ($x_{split} = 3L/4 = 22.5\,km$) and a standard NHS solver at $t = \{12\,hr, 24\,hr\}$. The non-hydrostatic pressure corrector is set to $\delta p' = 0$ along the dividing boundary and the background velocity and density anomaly are $u_0 = 0.5\,m/s$ and $\rho'_o = 2\,kg/m^3$.

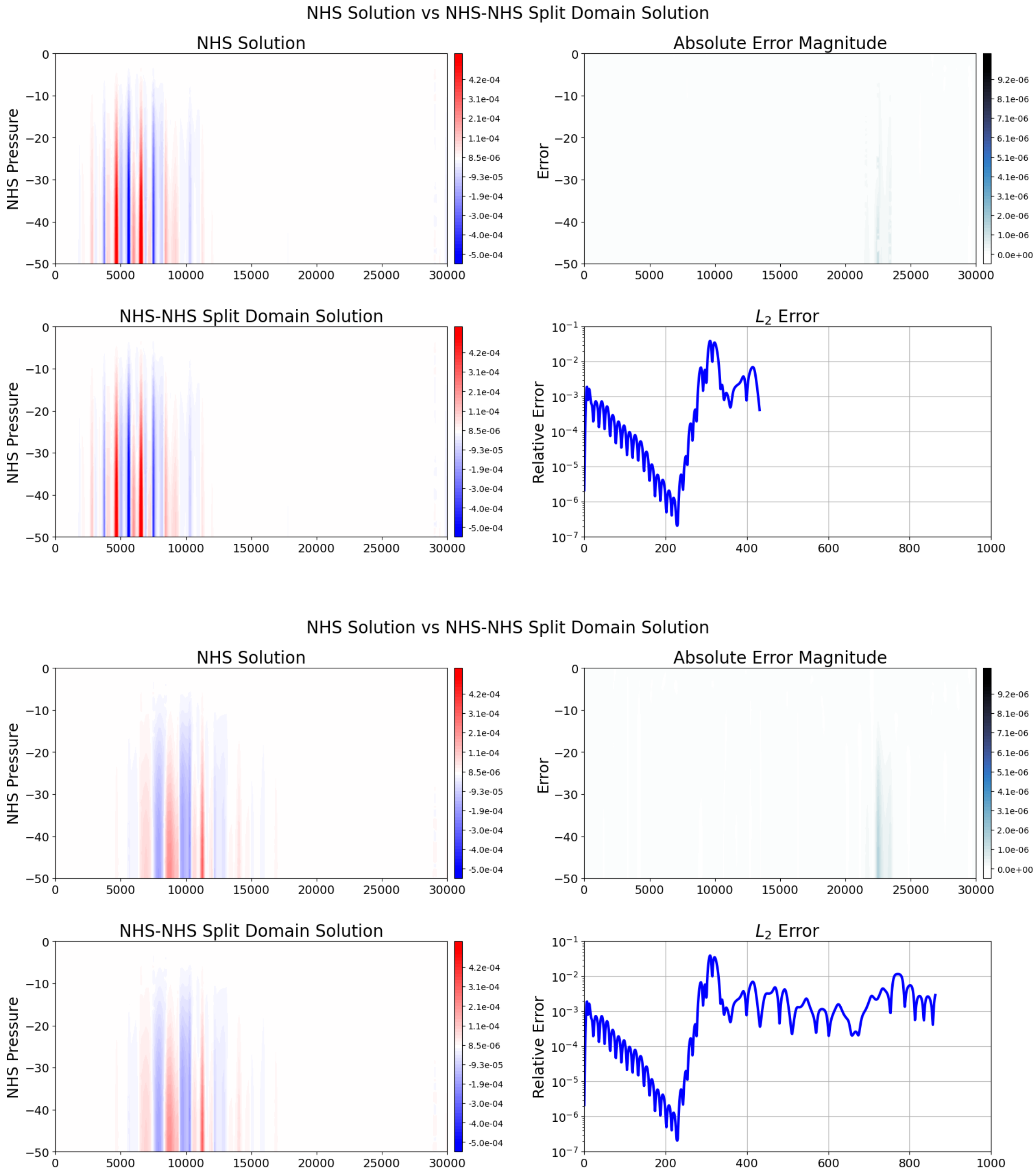

Figure 4-8: Comparison of the NHS pressure between a split-domain NHS-NHS solver ($x_{split} = 3L/4 = 22.5\,km$) and a standard NHS solver at $t = \{12\,hr, 24\,hr\}$. The non-hydrostatic pressure corrector is set to $\delta p' = 0$ along the dividing boundary and the background velocity and density anomaly are $u_0 = 0.5\,m/s$ and $\rho_o' = 2\,kg/m^3$.

Case 2: NHS-HS Split Domain

In this case, we use an NHS solver for the left subdomain ($0 < x < x_{split}$) and an HS solver for the right subdomain ($x_{split} < x < L$) and compare the resulting solution to the standard NHS solution. We impose a homogeneous boundary condition for the pressure corrector $\delta p' = 0$ along $x = x_{split}$ in the NHS subdomain. In addition to the error we introduced in case 1, we have introduced a hydrostatic approximation for the flow in the right subdomain.

Figure 4-9-4-10 show the density perturbation and NHS pressure profiles at $t = 12\,hr$ and $t = 24\,hr$ along with the absolute errors incurred by the split-domain solver. We see that although the relative error has now increased, it is restricted to about 1% for the density perturbation and to 10% for the NHS pressure. Similarly, we find that the relative error of the horizontal velocity is less than 1% and that of the vertical velocity is less than 10%. Furthermore, the primary flow features seem to be captured, and we see that the errors remain bounded at late times. Unlike the NHS-NHS split domain solver, significant errors are seen to propagate upstream of the domain. A timing analysis showed that the split-domain NHS-HS solver produced a computational saving of about 20% compared to the standard NHS solver. We note that the computational savings depend on how much of the domain exhibits NHS behaviour and for a more realistic large-scale problem with localized NHS effects, we can expect even greater computational savings.

We now repeat this simulation to investigate the effects of boundary condition choice by imposing different boundary conditions along the $x = x_{split}$ boundary within the NHS subdomain. Figure 4-11 illustrates the resulting error curves and we do not see a significant difference between the three cases. Since we have static subdomains initialized to a stratified field, we see that imposing the homogeneous Dirichlet condition $\delta p'^{,k+1} = 0$ and the previous timestep value condition $\delta p'^{,k+1} = \delta p'^{,k}$ results in the exact same solution. We note that it would be more interesting and informative to compare these boundary conditions in the context of an adaptive version of this algorithm where the subdomains are evolved in time as the simulation progresses such that subdomains can switch between the NHS and HS models.

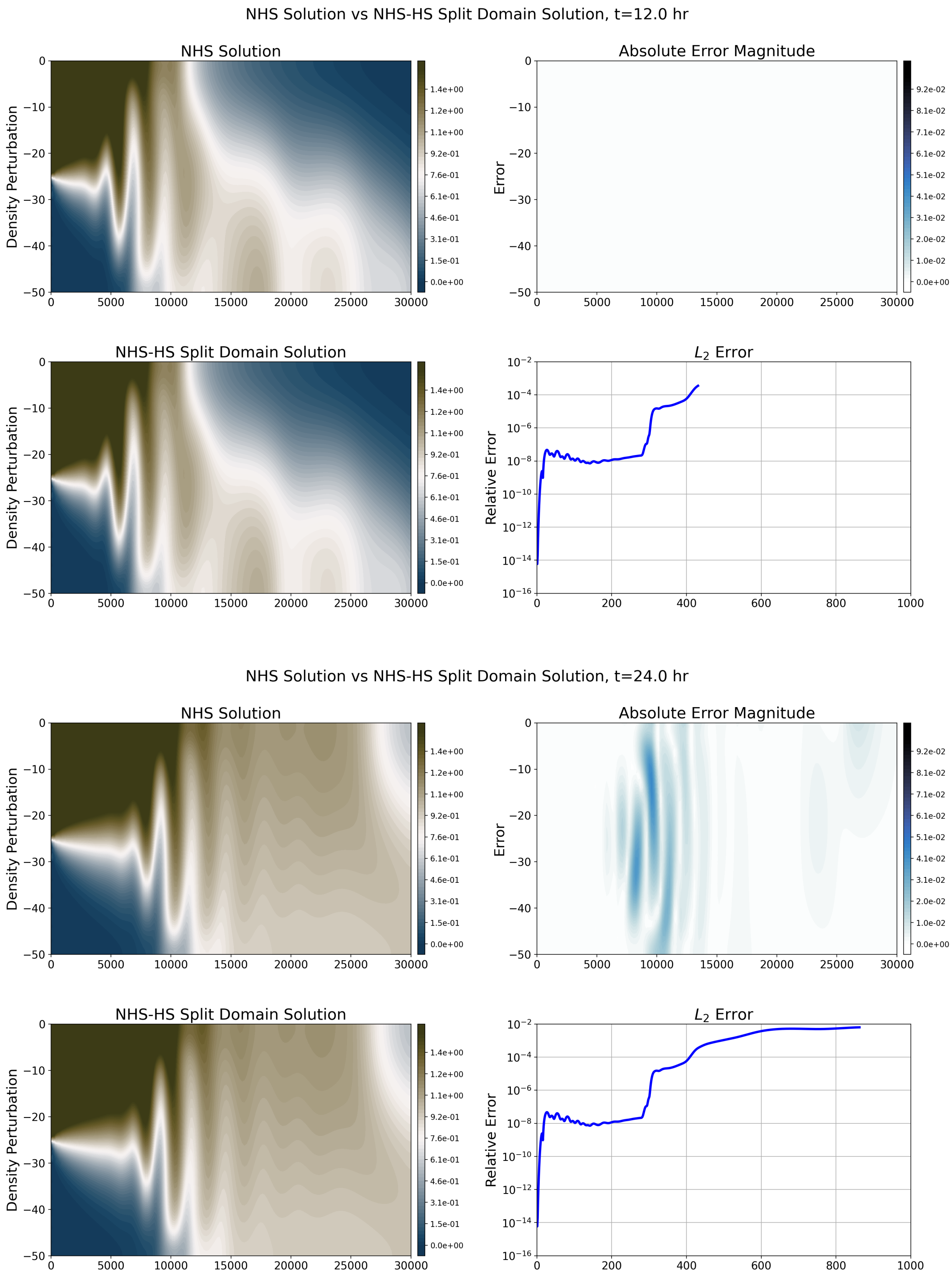

Figure 4-9: Comparison of the density perturbation between a split-domain NHS-HS solver ($x_{split} = 3L/4 = 22.5\,km$) and a standard NHS solver at $t = \{12\,hr, 24\,hr\}$. The non-hydrostatic pressure corrector is set to $\delta p' = 0$ along the dividing boundary and the background velocity and density anomaly are $u_0 = 0.5\,m/s$ and $\rho'_o = 2\,kg/m^3$.

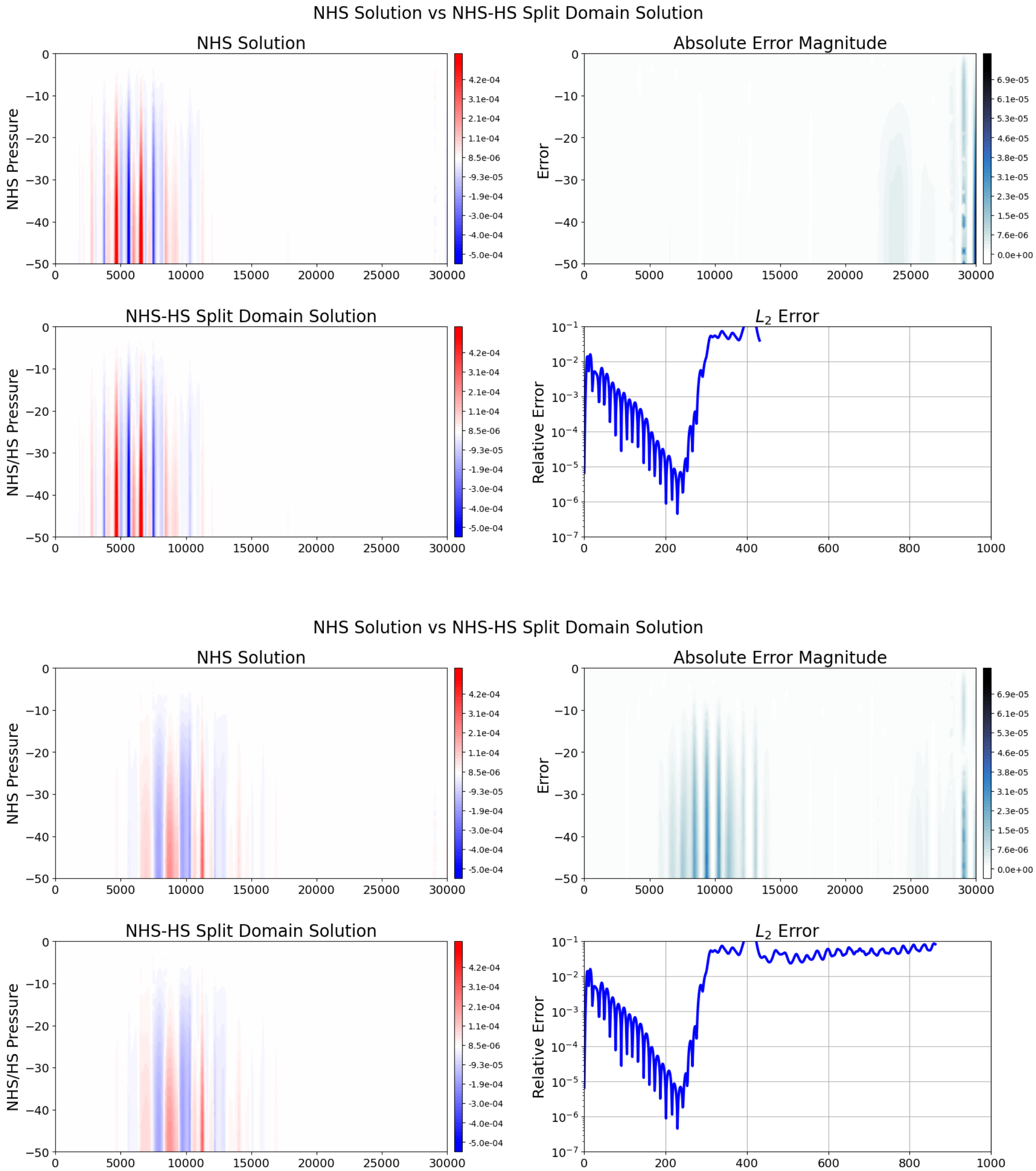

Figure 4-10: Comparison of the NHS pressure between a split-domain NHS-HS solver ($x_{split} = 3L/4 = 22.5\,km$) and a standard NHS solver at $t = \{12\,hr, 24\,hr\}$. The non-hydrostatic pressure corrector is set to $\delta p' = 0$ along the dividing boundary and the background velocity and density anomaly are $u_0 = 0.5\,m/s$ and $\rho'_o = 2\,kg/m^3$.

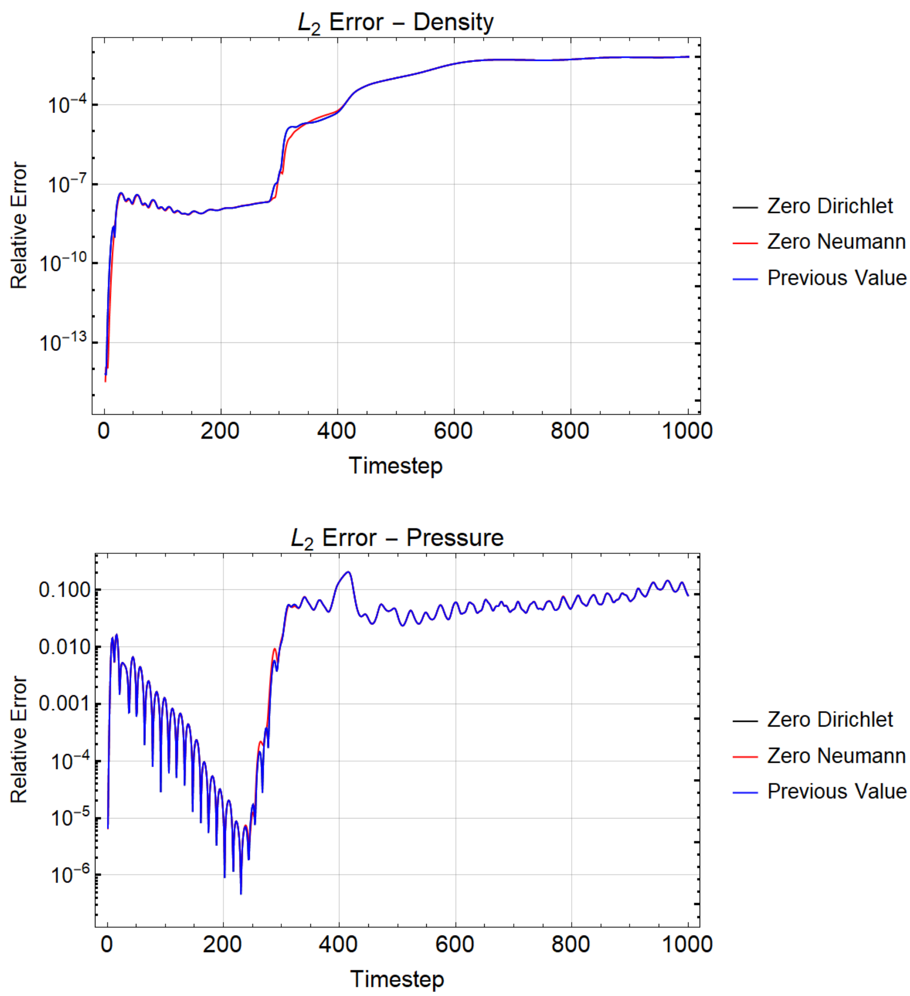

Figure 4-11: Comparison of the errors corresponding to the three boundary condition choices discussed in Section 3.1.2 for the density perturbation (top) and non-hydrostatic pressure (bottom). We note that the black and blue lines, corresponding to the homogeneous Dirichlet and previous timestep value boundary conditions, coincide here.

4.5 NHS Parameters

As we have discussed in the previous chapter, there are a few non-dimensional numbers that can potentially be used to predict non-hydrostatic behaviour. Here, we look at the numerical non-hydrostatic parameter defined as,

$$\alpha = \frac{\nabla_{xy} \cdot \underline{\bar{\bar{u}}}^{k+1}}{a\Delta t} + \frac{\nabla_{z} \cdot \underline{\bar{\bar{w}}}^{k+1}}{a\Delta t} \tag{4.2}$$

In Fig.4-12, we compare the NHS parameter α (scaled divergence of the velocity predictor) with the NHS pressure corrector $\delta p'$. We see that the NHS parameter is able to track domain regions with non-zero NHS pressure corrector values well throughout the simulation. Therefore, we can make use of this parameter to develop an adaptive algorithm as shown in Algorithm 3. Consider a domain split into multiple subdomains and initially tagged to be either non-hydrostatic or hydrostatic.

Algorithm 3 Adaptive Multi-dynamics Model

At each timestep, for each subdomain,
if Non-hydrostatic subdomain **then**
    if $p' <$ tolerance and $\alpha <$ tolerance **then**
        Switch subdomain tag to hydrostatic
    end if
else
    if $\alpha >$ tolerance **then**
        Switch subdomain tag to non-hydrostatic
    end if
end if

We can adjust the tolerance used as thresholds for transition between the NHS and HS models to choose between computational savings and accuracy. We are currently working on implementing this adaptive multi-dynamics model.

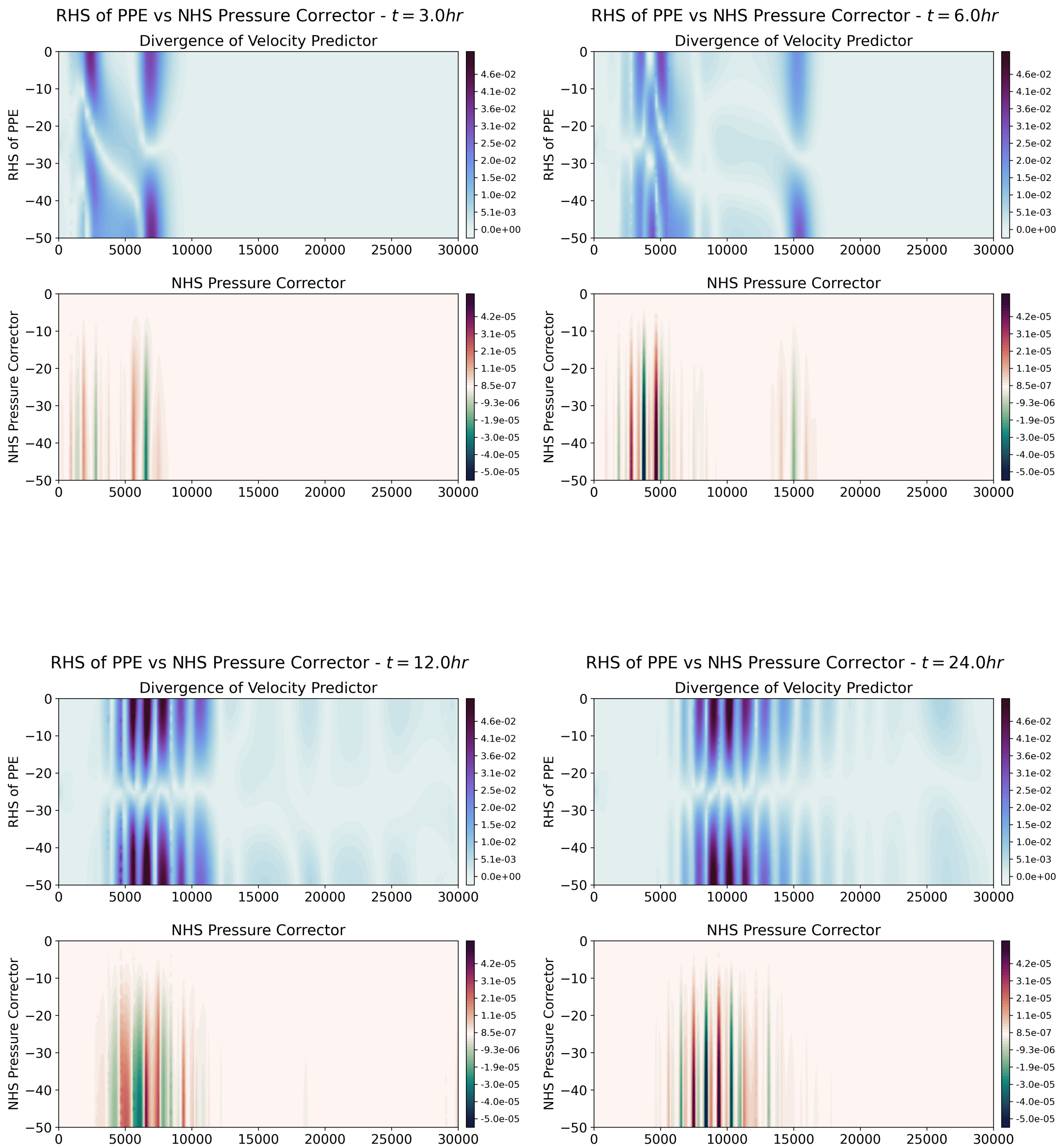

Figure 4-12: Plots of the non-hydrostatic pressure corrector and the divergence of the velocity predictor at $t = \{3\,hr, 6\,hr, 12\,hr, 24\,hr\}$. We see that the divergence of the velocity predictor can track the non-hydrostatic pressure corrector throughout the simulation.

Chapter 5

Conclusion and Future Work

This work presents a projection method-based multi-dynamics model for coupling the non-hydrostatic and hydrostatic ocean equations in the hybridizable discontinuous Galerkin [77] finite element method framework. The proposed model employs dynamics-appropriate models for different parts of the domain and therefore has the potential to optimally reduce the computational cost by resolving non-hydrostatic dynamics only where and when needed. We have detailed the implementation aspects associated with this model, emphasising possible boundary condition treatment. Timing analyses of our in-house, parallelized, C++ non-hydrostatic HDG solver [30, 33] are conducted to verify that computing the non-hydrostatic pressure is the computational bottleneck.

A first implementation of the multi-dynamics modeling system, with static subdomains, was developed. It was evaluated in the context of 2D idealized Rayleigh-Taylor instability-driven striations, inspired by ocean dynamics in multiple regions including the Mediterranean Sea (Alboran and Balearic Seas) and Gulf of Mexico. Simulation results were presented with discussions on accuracy evaluations and computational savings. We then discussed and obtained numerical parameters that could be used to quantify and anticipate non-hydrostatic behaviour within the domain locally. Our numerical experiments reveal that the divergence of the velocity predictor can be used to track regions with non-zero non-hydrostatic pressure.

We are working on an extension to this work where we devise an adaptive algorithm that uses the proposed parameter to track non-hydrostatic behaviour to dynamically choose regions where the NHS model is needed as the simulation evolves. Integrating this multi-dynamics algorithm with adaptive mesh refinement schemes [32] in the HDG framework could prove to be an effective method to optimize NHS simulations.

Research in the direction of novel numerical schemes and modern-day computing tools is critical in the pursuit of capturing and understanding a broad range of non-hydrostatic ocean phenomena. One route could be incorporating reduced-order methods within our HDG ocean modelling framework to reduce the memory requirement. The discovery of effective preconditioners and novel solution methods for the linear systems arising from HDG discretization is another avenue we are interested in. In particular, we are looking at multigrid methods [9, 17, 68] as they offer the attractive possibility of solving linear systems at a mesh size-independent rate. More sophisticated parameterization of sub-grid processes would go a long way in enabling large-scale realistic ocean simulations. Present-day data-driven approaches and parallel computing with graphics processing units (GPUs) have gained a lot of attention recently and they could also prove useful in tackling the computational challenge posed by non-hydrostatic simulations.

Advances towards efficient NHS simulations would enhance the capabilities of our Multidisciplinary Simulation, Estimation and Assimilation Systems (MSEAS) [75, 41, 38, 39] ocean modelling to perform realistic simulations and forecasts across the world's oceans, several of which have localized non-hydrostatic dynamics [47, 46, 60, 64, 63, 40, 42]. Such localized effects are also often important for underwater sound propagation and computational ocean acoustics [93, 28, 5, 3, 4]. Their simulations may also benefit from reduced-order modeling [13, 14], uncertainty quantification [59, 58], and data assimilation and adaptive sampling [66, 57, 65, 61].

Bibliography

[1] Coherent Lagrangian Pathways from the Surface Ocean to Interior (CALYPSO) - MSEAS Group Page.

[2] Emmanuel Agullo, Luc Giraud, Alexis GobÃ©, Matthieu Kuhn, StÃ©phane Lanteri, and Ludovic Moya. High order HDG method and domain decomposition solvers for frequency-domain electromagnetics. *International Journal of Numerical Modelling: Electronic Networks, Devices and Fields*, 33(2):e2678, 2020. _eprint: https://onlinelibrary.wiley.com/doi/pdf/10.1002/jnm.2678.

[3] Wael Hajj Ali, Manmeet S. Bhabra, Pierre F. J. Lermusiaux, Andrew March, Joseph R. Edwards, Katherine Rimpau, and Paul Ryu. Stochastic oceanographic-acoustic prediction and Bayesian inversion for wide area ocean floor mapping. In *OCEANS 2019 MTS/IEEE SEATTLE*, pages 1–10, Seattle, October 2019. IEEE.

[4] Wael Hajj Ali and Pierre F. J. Lermusiaux. Dynamically orthogonal narrow-angle parabolic equations for stochastic underwater sound propagation. *Journal of the Acoustical Society of America*, 2023. Sub-judice.

[5] Wael Hajj Ali, Mohamad H. Mirhi, Abhinav Gupta, Chinmay S. Kulkarni, Corbin Foucart, Manan M. Doshi, Deepak N. Subramani, Chris Mirabito, Patrick J. Haley, Jr., and Pierre F. J. Lermusiaux. Seavizkit: Interactive maps for ocean visualization. In *OCEANS 2019 MTS/IEEE SEATTLE*, pages 1–10, Seattle, October 2019. IEEE.

[6] Jean Aoussou, Jing Lin, and Pierre F. J. Lermusiaux. Iterated pressure-correction projection methods for the unsteady incompressible Navier–Stokes equations. *Journal of Computational Physics*, 373:940–974, November 2018.

[7] F. Auclair, L. Bordois, Y. Dossmann, T. Duhaut, A. Paci, C. Ulses, and C. Nguyen. A non-hydrostatic non-Boussinesq algorithm for free-surface ocean modelling. *Ocean Modelling*, 132:12–29, December 2018.

[8] Guido Boffetta and Andrea Mazzino. Incompressible Rayleigh-Taylor Turbulence. *Annual Review of Fluid Mechanics*, 49(1):119–143, 2017. _eprint: https://doi.org/10.1146/annurev-fluid-010816-060111.

[9] James H. Bramble. *Multigrid methods*. Chapman and Hall/CRC, New York, November 2019.

[10] M. C. Buijsman, Y. Kanarska, and J. C. McWilliams. On the generation and evolution of nonlinear internal waves in the South China Sea. *Journal of Geophysical Research: Oceans*, 115(C2), 2010. _eprint: https://onlinelibrary.wiley.com/doi/pdf/10.1029/2009JC005275.

[11] V. Casulli and P. Zanolli. Semi-implicit numerical modeling of nonhydrostatic free-surface flows for environmental problems. *Mathematical and Computer Modelling*, 36(9):1131–1149, December 2002.

[12] Vincenzo Casulli. A semi-implicit finite difference method for non-hydrostatic, free-surface flows. *International Journal for Numerical Methods in Fluids*, 30(4):425–440, 1999. _eprint: https://onlinelibrary.wiley.com/doi/pdf/10.1002/%28SICI%291097-0363%2819990630%2930%3A4%3C425%3A%3AAID-FLD847%3E3.0.CO%3B2-D.

[13] Aaron Charous and Pierre F. J. Lermusiaux. Dynamically orthogonal differential equations for stochastic and deterministic reduced-order modeling of ocean acoustic wave propagation. In *OCEANS 2021 IEEE/MTS*, pages 1–7. IEEE, September 2021.

[14] Aaron Charous and Pierre F. J. Lermusiaux. Dynamically orthogonal Runge–Kutta schemes with perturbative retractions for the dynamical low-rank approximation. *SIAM Journal on Scientific Computing*, 45(2):A872–A897, 2023.

[15] Changsheng Chen, Hedong Liu, and Robert C. Beardsley. An Unstructured Grid, Finite-Volume, Three-Dimensional, Primitive Equations Ocean Model: Application to Coastal Ocean and Estuaries. *Journal of Atmospheric and Oceanic Technology*, 20(1):159–186, January 2003. Publisher: American Meteorological Society Section: Journal of Atmospheric and Oceanic Technology.

[16] Alexandre Joel Chorin. Numerical solution of the Navier-Stokes equations. *Mathematics of Computation*, 22(104):745–762, 1968.

[17] B. Cockburn, O. Dubois, J. Gopalakrishnan, and S. Tan. Multigrid for an HDG method. *IMA Journal of Numerical Analysis*, 34(4):1386–1425, October 2014.

[18] Bernardo Cockburn and Jayadeep Gopalakrishnan. The Derivation of Hybridizable Discontinuous Galerkin Methods for Stokes Flow. *SIAM Journal on Numerical Analysis*, 47(2):1092–1125, January 2009. Publisher: Society for Industrial and Applied Mathematics.

[19] Bernardo Cockburn, Jayadeep Gopalakrishnan, and Raytcho Lazarov. Unified Hybridization of Discontinuous Galerkin, Mixed, and Continuous Galerkin Methods for Second Order Elliptic Problems. *SIAM Journal on Numerical Analysis*, 47(2):1319–1365, January 2009. Publisher: Society for Industrial and Applied Mathematics.

[20] Benoit Cushman-Roisin and Jean-Marie Beckers. *Introduction to Geophysical Fluid Dynamics: Physical and Numerical Aspects*. Academic Press, August 2011. Google-Books-ID: 3KS8sD5ky9kC.

[21] Stuart B. Dalziel. Rayleigh-Taylor instability: experiments with image analysis. *Dynamics of Atmospheres and Oceans*, 20(1):127–153, November 1993.

[22] M. K. Davey and J. A. Whitehead. Rotating rayleigh-taylor instability as a model of sinking events in the ocean. *Geophysical & Astrophysical Fluid Dynamics*, 17(1):237–253, January 1981. Publisher: Taylor & Francis _eprint: https://doi.org/10.1080/03091928108243684.

[23] Eric Deleersnijder, Vincent Legat, and Pierre F. J. Lermusiaux. Multi-scale modelling of coastal, shelf and global ocean dynamics. *Ocean Dynamics*, 60(6):1357–1359, December 2010.

[24] Eric Deleersnijder and Pierre F. J. Lermusiaux. Multi-scale modeling: nested-grid and unstructured-mesh approaches. *Ocean Dynamics*, 58(5–6):335–336, December 2008.

[25] B. Desjardins and E. Grenier. On Nonlinear Rayleigh-Taylor Instabilities. *Acta Mathematica Sinica*, 22(4):1007–1016, July 2006.

[26] Thomas Dobbelaere, Milan Curcic, Matthieu Le HÃ©naff, and Emmanuel Hanert. Impacts of Hurricane Irma (2017) on wave-induced ocean transport processes. *Ocean Modelling*, 171:101947, March 2022.

[27] T. F. Duda, Y.-T. Lin, A. E. Newhall, K. R. Helfrich, W. G. Zhang, M. Badiey, P. F. J. Lermusiaux, J. A. Colosi, and J. F. Lynch. The “Integrated Ocean Dynamics and Acoustics" (IODA) hybrid modeling effort. In *Proceedings of the international conference on Underwater Acoustics - 2014 (UA2014)*, pages 621–628, 2014.

[28] Timothy F. Duda, Ying-Tsong Lin, Arthur E. Newhall, Karl R. Helfrich, James F. Lynch, Weifeng Gordon Zhang, Pierre F. J. Lermusiaux, and John Wilkin. Multiscale multiphysics data-informed modeling for three-dimensional ocean acoustic simulation and prediction. *Journal of the Acoustical Society of America*, 146(3):1996–2015, September 2019.

[29] R. Ford, C. C. Pain, M. D. Piggott, A. J. H. Goddard, C. R. E. de Oliveira, and A. P. Umpleby. A Nonhydrostatic Finite-Element Model for Three-Dimensional Stratified Oceanic Flows. Part I: Model Formulation. *Monthly Weather Review*, 132(12):2816–2831, December 2004. Publisher: American Meteorological Society Section: Monthly Weather Review.

[30] C. Foucart, C. Mirabito, P. J. Haley, Jr., and P. F. J. Lermusiaux. Distributed implementation and verification of hybridizable discontinuous Galerkin methods for nonhydrostatic ocean processes. In *OCEANS Conference 2018*, Charleston, SC, October 2018. IEEE.

[31] Corbin Foucart. Efficient matrix-free implementation and automated verification of hybridizable discontinuous Galerkin finite element methods. Master's thesis, Massachusetts Institute of Technology, Department of Mechanical Engineering, Cambridge, Massachusetts, June 2019.

[32] Corbin Foucart, Aaron Charous, and Pierre F. J. Lermusiaux. Deep reinforcement learning for adaptive mesh refinement. *Journal of Computational Physics*, 2023. Sub-judice.

[33] Corbin Foucart, Chris Mirabito, Patrick J. Haley, Jr., and Pierre F. J. Lermusiaux. High-order discontinuous Galerkin methods for nonhydrostatic ocean processes with a free surface. In *OCEANS 2021 IEEE/MTS*, pages 1–9. IEEE, September 2021.

[34] Baylor Fox-Kemper, Alistair Adcroft, Claus W. BÃ¶ning, Eric P. Chassignet, Enrique Curchitser, Gokhan Danabasoglu, Carsten Eden, Matthew H. England, RÃŒdiger Gerdes, Richard J. Greatbatch, Stephen M. Griffies, Robert W. Hallberg, Emmanuel Hanert, Patrick Heimbach, Helene T. Hewitt, Christopher N. Hill, Yoshiki Komuro, Sonya Legg, Julien Le Sommer, Simona Masina, Simon J. Marsland, Stephen G. Penny, Fangli Qiao, Todd D. Ringler, Anne Marie Treguier, Hiroyuki Tsujino, Petteri Uotila, and Stephen G. Yeager. Challenges and Prospects in Ocean Circulation Models. *Frontiers in Marine Science*, 6, 2019.

[35] O. B. Fringer, M. Gerritsen, and R. L. Street. An unstructured-grid, finite-volume, nonhydrostatic, parallel coastal ocean simulator. *Ocean Modelling*, 14(3):139–173, January 2006.

[36] Martin J. Gander. Optimized Schwarz Methods. *SIAM Journal on Numerical Analysis*, 44(2):699–731, January 2006. Publisher: Society for Industrial and Applied Mathematics.

[37] Thomas W. N Haine and Paul D Williams. The role of nonhydrostatic dynamics in controlling development of a surface ocean front. *Ocean Modelling*, 4(2):121–135, January 2002.

[38] P. J. Haley, Jr., A. Agarwal, and P. F. J. Lermusiaux. Optimizing velocities and transports for complex coastal regions and archipelagos. *Ocean Modeling*, 89:1–28, 2015.

[39] P. J. Haley, Jr., P. F. J. Lermusiaux, A. R. Robinson, W. G. Leslie, O. Logoutov, G. Cossarini, X. S. Liang, P. Moreno, S. R. Ramp, J. D. Doyle, J. Bellingham, F. Chavez, and S. Johnston. Forecasting and reanalysis in the Monterey Bay/California Current region for the Autonomous Ocean Sampling Network-II experiment. *Deep Sea Research Part II: Topical Studies in Oceanography*, 56(3–5):127–148, February 2009.

[40] Patrick J. Haley, Jr., Abhinav Gupta, Chris Mirabito, and Pierre F. J. Lermusiaux. Towards Bayesian ocean physical-biogeochemical-acidification prediction and learning systems for Massachusetts Bay. In *OCEANS 2020 IEEE/MTS*, pages 1–9. IEEE, October 2020.

[41] Patrick J. Haley, Jr. and Pierre F. J. Lermusiaux. Multiscale two-way embedding schemes for free-surface primitive equations in the "Multidisciplinary Simulation, Estimation and Assimilation System". *Ocean Dynamics*, 60(6):1497–1537, December 2010.

[42] Patrick J. Haley, Jr., Chris Mirabito, Manan Doshi, and Pierre F. J. Lermusiaux. Ensemble forecasting for the Gulf of Mexico Loop Current region. In *OCEANS 2023 IEEE/MTS Gulf Coast*, Biloxi, MS, September 2023. IEEE. Sub-judice.

[43] Emmanuel Hanert, Aboobacker Valliyil Mohammed, Subramanian Veerasingam, Thomas Dobbelaere, Valentin Vallaeys, and Ponnumony Vethamony. A multiscale ocean modelling system for the central Arabian/Persian Gulf: From regional to structure scale circulation patterns. *Estuarine, Coastal and Shelf Science*, 282:108230, March 2023.

[44] Jan Hesthaven and Tim Warburton. Nodal Discontinuous Galerkin Methods: Algorithms, Analysis, and Applications. volume 54. January 2007.

[45] Ben R. Hodges, Bernard Laval, and Bridget M. Wadzuk. Numerical error assessment and a temporal horizon for internal waves in a hydrostatic model. *Ocean Modelling*, 13(1):44–64, January 2006.

[46] T. M. S. Johnston, J. A. MacKinnon, P. L. Colin, P. J. Haley, Jr., P. F. J. Lermusiaux, A. J. Lucas, M. A. Merrifield, S. T. Merrifield, C. Mirabito, J. D. Nash, C. Y. Ou, M. Siegelman, E. J. Terrill, and A. F. Waterhouse. Energy and momentum lost to wake eddies and lee waves generated by the North Equatorial Current and tidal flows at Peleliu, Palau. *Oceanography*, 32(4):110–125, December 2019.

[47] T. M. S. Johnston, M. C. Schönau, T. Paluszkiewicz, J. A. MacKinnon, B. K. Arbic, P. L. Colin, M. H. Alford, M. Andres, L. Centurioni, H. C. Graber, K. R. Helfrich, V. Hormann, P. F. J. Lermusiaux, R. C. Musgrave, B. S. Powell, B. Qiu, D. L. Rudnick, H. L. Simmons, L. St. Laurent, E. J. Terrill, D. S. Trossman, G. Voet, H. W. Wijesekera, and K. L. Zeiden. Flow Encountering Abrupt Topography (FLEAT): A multiscale observational and modeling program to understand how topography affects flows in the western North Pacific. *Oceanography*, 32(4):10–21, December 2019.

[48] Y. Kanarska, A. Shchepetkin, and J. C. McWilliams. Algorithm for non-hydrostatic dynamics in the Regional Oceanic Modeling System. *Ocean Modelling*, 18(3):143–174, January 2007.

[49] Lakshmi H. Kantha and Carol Anne Clayson. *Small Scale Processes in Geophysical Fluid Flows*. Elsevier, August 2000. Google-Books-ID: c9BsNjRd9oYC.

[50] S. M. Kelly and P. F. J. Lermusiaux. Internal-tide interactions with Gulf Stream and Middle Atlantic Bight shelfbreak front. *Journal of Geophysical Research: Oceans*, 121:6271–6294, 2016.

[51] S. M. Kelly, P. F. J. Lermusiaux, T. F. Duda, and P. J. Haley, Jr. A coupled-mode shallow water model for tidal analysis: Internal-tide reflection and refraction by the Gulf Stream. *Journal of Physical Oceanography*, 46:3661–3679, 2016.

[52] Knut Klingbeil and Hans Burchard. Implementation of a direct nonhydrostatic pressure gradient discretisation into a layered ocean model. *Ocean Modelling*, 65:64–77, May 2013.

[53] H. J. Kull. Theory of the Rayleigh-Taylor instability. *Physics Reports*, 206(5):197–325, August 1991.

[54] Robert Jan Labeur and Julie D. Pietrzak. A fully three dimensional unstructured grid non-hydrostatic finite element coastal model. *Ocean Modelling*, 10(1):51–67, January 2005.

[55] Zhigang Lai, Changsheng Chen, Geoffrey W. Cowles, and Robert C. Beardsley. A nonhydrostatic version of FVCOM: 1. Validation experiments. *Journal of Geophysical Research: Oceans*, 115(C11), 2010. _eprint: https://onlinelibrary.wiley.com/doi/pdf/10.1029/2009JC005525.

[56] Zhigang Lai, Changsheng Chen, Geoffrey W. Cowles, and Robert C. Beardsley. A nonhydrostatic version of FVCOM: 2. Mechanistic study of tidally generated nonlinear internal waves in Massachusetts Bay. *Journal of Geophysical Research: Oceans*, 115(C12), 2010. _eprint: https://onlinelibrary.wiley.com/doi/pdf/10.1029/2010JC006331.

[57] P. F. J. Lermusiaux. Data assimilation via Error Subspace Statistical Estimation, part II: Mid-Atlantic Bight shelfbreak front simulations, and ESSE validation. *Monthly Weather Review*, 127(7):1408–1432, July 1999.

[58] P. F. J. Lermusiaux. Uncertainty estimation and prediction for interdisciplinary ocean dynamics. *Journal of Computational Physics*, 217(1):176–199, 2006.

[59] P. F. J. Lermusiaux, C.-S. Chiu, G. G. Gawarkiewicz, P. Abbot, A. R. Robinson, R. N. Miller, P. J. Haley, Jr, W. G. Leslie, S. J. Majumdar, A. Pang, and F. Lekien. Quantifying uncertainties in ocean predictions. *Oceanography*, 19(1):92–105, 2006.

[60] P. F. J Lermusiaux, A. J. Miller, and N. Pinardi. Special issue of Dynamics of Atmospheres and Oceans in honor of Prof. A. R. Robinson. *Dynamics of Atmospheres and Oceans*, 52(1–2):1–3, September 2011. Editorial.

[61] P. F. J. Lermusiaux, D. N. Subramani, J. Lin, C. S. Kulkarni, A. Gupta, A. Dutt, T. Lolla, P. J. Haley, Jr., W. H. Ali, C. Mirabito, and S. Jana. A future for intelligent autonomous ocean observing systems. *Journal of Marine Research*, 75(6):765–813, November 2017. The Sea. Volume 17, The Science of Ocean Prediction, Part 2.

[62] Pierre F. J. Lermusiaux. Numerical fluid mechanics. MIT OpenCourseWare, May 2015.

[63] Pierre F. J. Lermusiaux, Manan Doshi, Chinmay S. Kulkarni, Abhinav Gupta, Patrick J. Haley, Jr., Chris Mirabito, Francesco Trotta, S. J. Levang, G. R. Flierl, J. Marshall, Thomas Peacock, and C. Noble. Plastic pollution in the coastal oceans: Characterization and modeling. In *OCEANS 2019 MTS/IEEE SEATTLE*, pages 1–10, Seattle, October 2019. IEEE.

[64] Pierre F. J. Lermusiaux, Patrick J. Haley, Jr., Chris Mirabito, Wael H. Ali, Manmeet Bhabra, Phil Abbot, Ching-Sang Chiu, and Chris Emerson. Multi-resolution probabilistic ocean physics-acoustic modeling: Validation in the New Jersey continental shelf. In *OCEANS 2020 IEEE/MTS*, pages 1–9. IEEE, October 2020.

[65] Pierre F. J. Lermusiaux, P. Malanotte-Rizzoli, D. Stammer, J. Carton, J. Cummings, and A. M. Moore. Progress and prospects of U.S. data assimilation in ocean research. *Oceanography*, 19(1):172–183, 2006.

[66] Pierre F. J. Lermusiaux and A. R. Robinson. Data assimilation via Error Subspace Statistical Estimation, part I: Theory and schemes. *Monthly Weather Review*, 127(7):1385–1407, 1999.

[67] Liang Li, StÃ©phane Lanteri, and Ronan Perrussel. A hybridizable discontinuous Galerkin method combined to a Schwarz algorithm for the solution of 3d time-harmonic MaxwellÊŒs equation. *Journal of Computational Physics*, 256:563–581, January 2014.

[68] Peipei Lu, Andreas Rupp, and Guido Kanschat. Homogeneous multigrid for HDG. *IMA Journal of Numerical Analysis*, page drab055, July 2021.

[69] Gangfeng Ma, Fengyan Shi, and James T. Kirby. Shock-capturing non-hydrostatic model for fully dispersive surface wave processes. *Ocean Modelling*, 43-44:22–35, January 2012.

[70] Amala Mahadevan, Joseph Oliger, and Robert Street. A Nonhydrostatic Mesoscale Ocean Model. Part I: Well-Posedness and Scaling. *Journal of Physical Oceanography*, 26(9):1868–1880, September 1996. Publisher: American Meteorological Society Section: Journal of Physical Oceanography.

[71] Amala Mahadevan, Joseph Oliger, and Robert Street. A Nonhydrostatic Mesoscale Ocean Model. Part II: Numerical Implementation. *Journal of Physical Oceanography*, 26(9):1881–1900, September 1996. Publisher: American Meteorological Society Section: Journal of Physical Oceanography.

[72] John Marshall, Alistair Adcroft, Chris Hill, Lev Perelman, and Curt Heisey. A finite-volume, incompressible Navier Stokes model for studies of the ocean on parallel computers. *Journal of Geophysical Research: Oceans*, 102(C3):5753–5766, 1997. _eprint: https://onlinelibrary.wiley.com/doi/pdf/10.1029/96JC02775.

[73] John Marshall, Chris Hill, Lev Perelman, and Alistair Adcroft. Hydrostatic, quasi-hydrostatic, and nonhydrostatic ocean modeling. *Journal of Geophysical Research: Oceans*, 102(C3):5733–5752, 1997. _eprint: https://onlinelibrary.wiley.com/doi/pdf/10.1029/96JC02776.

[74] A. J. Molcard, N. Pinardi, and R. Ansaloni. A Spectral Element Ocean Model on the Cray T3D: the interannual variability of the Mediterranean Sea general circulation. *Physics and Chemistry of the Earth*, 23(5):491–495, January 1998.

[75] MSEAS Group. MSEAS Software, 2013.

[76] Cuong Nguyen, Xevi Roca, David Moro, and Jaime Peraire. A Hybridized Multiscale Discontinuous Galerkin Method for Compressible Flows. In *51st AIAA Aerospace Sciences Meeting including the New Horizons Forum and Aerospace Exposition*, Aerospace Sciences Meetings. American Institute of Aeronautics and Astronautics, January 2013.

[77] N. C. Nguyen, J. Peraire, and B. Cockburn. An implicit high-order hybridizable discontinuous Galerkin method for linear convection-diffusion equations. *Journal of Computational Physics*, 228(9):3232–3254, May 2009.

[78] N. C. Nguyen, J. Peraire, and B. Cockburn. An implicit high-order hybridizable discontinuous Galerkin method for nonlinear convection-diffusion equations. *Journal of Computational Physics*, 228(23):8841–8855, December 2009.

[79] N. C. Nguyen, J. Peraire, and B. Cockburn. A hybridizable discontinuous Galerkin method for Stokes flow. *Computer Methods in Applied Mechanics and Engineering*, 199(9):582–597, January 2010.

[80] N. C. Nguyen, J. Peraire, and B. Cockburn. Hybridizable discontinuous Galerkin methods for the time-harmonic Maxwell's equations. *Journal of Computational Physics*, 230(19):7151–7175, August 2011.

[81] Tien-Tai Nguyen. Nonlinear Rayleigh-Taylor instability of the viscous surface wave in an infinitely deep ocean, November 2022. arXiv:2211.14888 [math].

[82] Wei Pan, Stephan C. Kramer, and Matthew D. Piggott. Multi-layer non-hydrostatic free surface modelling using the discontinuous Galerkin method. *Ocean Modelling*, 134:68–83, February 2019.

[83] Wei Pan, Stephan C. Kramer, and Matthew D. Piggott. A σ-coordinate non-hydrostatic discontinuous finite element coastal ocean model. *Ocean Modelling*, 157:101732, January 2021.

[84] Jaime Peraire, Cuong Nguyen, and Bernardo Cockburn. An Embedded Discontinuous Galerkin Method for the Compressible Euler and Navier-Stokes Equations. In *20th AIAA Computational Fluid Dynamics Conference*, Fluid Dynamics and Co-located Conferences. American Institute of Aeronautics and Astronautics, June 2011.

[85] Jaime Peraire, Ngoc Nguyen, and Bernardo Cockburn. A Hybridizable Discontinuous Galerkin Method for the Compressible Euler and Navier-Stokes Equations. In *48th AIAA Aerospace Sciences Meeting Including the New Horizons Forum and Aerospace Exposition*, Aerospace Sciences Meetings. American Institute of Aeronautics and Astronautics, January 2010.

[86] J. Pianezze, C. Barthe, S. Bielli, P. Tulet, S. Jullien, G. Cambon, O. Bousquet, M. Claeys, and E. Cordier. A New Coupled Ocean Waves Atmosphere Model Designed for Tropical Storm Studies: Example of Tropical Cyclone Bejisa (2013-2014) in the SouthWest Indian Ocean. *Journal of Advances in Modeling Earth Systems*, 10(3):801–825, 2018. _eprint: https://onlinelibrary.wiley.com/doi/pdf/10.1002/2017MS001177.

[87] M. D. Piggott, C. C. Pain, G. J. Gorman, P. W. Power, and A. J. H. Goddard. h, r, and hr adaptivity with applications in numerical ocean modelling. *Ocean Modelling*, 10(1):95–113, January 2005.

[88] Matthew D. Piggott, Christopher C. Pain, Gerard J. Gorman, David P. Marshall, and Peter D. Killworth. Unstructured Adaptive Meshes for Ocean Modeling. In *Ocean Modeling in an Eddying Regime*, pages 383–408. American Geophysical Union (AGU), 2008. _eprint: https://onlinelibrary.wiley.com/doi/pdf/10.1029/177GM22.

[89] Nadia Pinardi, L. Cavaleri, G. Coppini, P. De Mey, C. Fratianni, J. Huthnance, P. F. J. Lermusiaux, A. Navarra, R. Preller, and S. Tibaldi. From weather to ocean predictions: an historical viewpoint. *Journal of Marine Research*, 75(3):103–159, May 2017. Special issue: The Science of Ocean Prediction, vol. 17 of The Sea.

[90] Nadia Pinardi, P. F. J. Lermusiaux, K. H. Brink, and R. Preller. The sea: The science of ocean prediction. *Journal of Marine Research*, 75(3):101–102, May 2017. Special issue: The Science of Ocean Prediction, vol. 17 of The Sea.

[91] Ali Ramadhan, Gregory LeClaire Wagner, Chris Hill, Jean-Michel Campin, Valentin Churavy, Tim Besard, Andre Souza, Alan Edelman, Raffaele Ferrari, and John Marshall. Oceananigans.jl: Fast and friendly geophysical fluid dynamics on GPUs. *Journal of Open Source Software*, 5(53):2018, September 2020.

[92] Bruce A. Remington, R. Paul Drake, Hideaki Takabe, and David Arnett. A review of astrophysics experiments on intense lasers. *Physics of Plasmas*, 7(5):1641–1652, May 2000.

[93] A. R. Robinson and P. F. J. Lermusiaux. Prediction systems with data assimilation for coupled ocean science and ocean acoustics. In A. Tolstoy et al, editor, *Proceedings of the Sixth International Conference on Theoretical and Computational Acoustics*, pages 325–342. World Scientific Publishing, 2004. Refereed invited Keynote Manuscript.

[94] Joko Sampurno, Valentin Vallaeys, Randy Ardianto, and Emmanuel Hanert. Modeling interactions between tides, storm surges, and river discharges in the Kapuas River delta. *Biogeosciences*, 19(10):2741–2757, June 2022. Publisher: Copernicus GmbH.

[95] Edward Santilli and Alberto Scotti. The Stratified Ocean Model with Adaptive Refinement (SOMAR). *Journal of Computational Physics*, 291:60–81, June 2015.

[96] Alexander F. Shchepetkin and James C. McWilliams. The regional oceanic modeling system (ROMS): a split-explicit, free-surface, topography-following-coordinate oceanic model. *Ocean Modelling*, 9(4):347–404, January 2005.

[97] Fengyan Shi, C. Chris Chickadel, Tian-Jian Hsu, James T. Kirby, Gordon Farquharson, and Gangfeng Ma. High-Resolution Non-Hydrostatic Modeling of Frontal Features in the Mouth of the Columbia River. *Estuaries and Coasts*, 40(1):296–309, January 2017.

[98] Barry Smith, Petter Bjorstad, and William Gropp. *Domain Decomposition: Parallel Multilevel Methods for Elliptic Partial Differential Equations*. Cambridge University Press, Cambridge, March 2004.

[99] S.-C. Soon, B. Cockburn, and Henryk K. Stolarski. A hybridizable discontinuous Galerkin method for linear elasticity. *International Journal for Numerical Methods in Engineering*, 80(8):1058–1092, 2009. _eprint: https://onlinelibrary.wiley.com/doi/pdf/10.1002/nme.2646.

[100] Qiang Tang, Xiaomeng Huang, Lei Lin, Wei Xiong, Dong Wang, Mingqing Wang, and Xing Huang. MERF v3.0, a highly computationally efficient non-hydrostatic ocean model with implicit parallelism: Algorithms and validation experiments. *Ocean Modelling*, 167:101877, November 2021.

[101] L. J. P. Timmermans, P. D. Minev, and F. N. Van De Vosse. An Approximate Projection Scheme for Incompressible Flow Using Spectral Elements. *International Journal for Numerical Methods in Fluids*, 22(7):673–688, 1996. _eprint: https://onlinelibrary.wiley.com/doi/pdf/10.1002/%28SICI%291097-0363%2819960415%2922%3A7%3C673%3A%3AAID-FLD373%3E3.0.CO%3B2-O.

[102] M. P. Ueckermann. Towards next generation ocean models: Novel discontinuous Galerkin schemes for 2D unsteady biogeochemical models. Master's thesis, Massachusetts Institute of Technology, Department of Mechanical Engineering, Cambridge, MA, September 2009.

[103] M. P. Ueckermann. *High Order Hybrid Discontinuous Galerkin Regional Ocean Modeling*. PhD thesis, Massachusetts Institute of Technology, Department of Mechanical Engineering, Cambridge, MA, February 2014.

[104] M. P. Ueckermann and P. F. J. Lermusiaux. High order schemes for 2D unsteady biogeochemical ocean models. *Ocean Dynamics*, 60(6):1415–1445, December 2010.

[105] M. P. Ueckermann and P. F. J. Lermusiaux. 2.29 Finite Volume MATLAB Framework Documentation. MSEAS Report 14, Department of Mechanical Engineering, Massachusetts Institute of Technology, Cambridge, MA, 2012.

[106] M. P. Ueckermann and P. F. J. Lermusiaux. Hybridizable discontinuous Galerkin projection methods for Navier–Stokes and Boussinesq equations. *Journal of Computational Physics*, 306:390–421, 2016.

[107] Mattheus P. Ueckermann, Chris Mirabito, Patrick J. Haley, Jr., and Pierre F. J. Lermusiaux. High order hybridizable discontinuous Galerkin projection schemes for non-hydrostatic physical-biogeochemical ocean modeling. *Ocean Dynamics*, 2023. In preparation.

[108] Valentin Vallaeys, Jonathan Lambrechts, Philippe Delandmeter, Johannes PÃ€tsch, Alejandro Spitzy, Emmanuel Hanert, and Eric Deleersnijder. Understanding the circulation in the deep, micro-tidal and strongly stratified Congo River estuary. *Ocean Modelling*, 167:101890, November 2021.

[109] Hans van Haren. Instability observations associated with wave breaking in the stable-stratified deep-ocean. *Physica D: Nonlinear Phenomena*, 292-293:62–69, February 2015.

[110] Sean Vitousek and Oliver B. Fringer. Physical vs. numerical dispersion in non-hydrostatic ocean modeling. *Ocean Modelling*, 40(1):72–86, January 2011.

[111] Sean Vitousek and Oliver B. Fringer. A nonhydrostatic, isopycnal-coordinate ocean model for internal waves. *Ocean Modelling*, 83:118–144, November 2014.

[112] David L. Youngs. Numerical simulation of turbulent mixing by Rayleigh-Taylor instability. *Physica D: Nonlinear Phenomena*, 12(1):32–44, July 1984.

[113] Ye Zhou. Rayleigh–Taylor and Richtmyer–Meshkov instability induced flow, turbulence, and mixing. I. *Physics Reports*, 720-722:1–136, December 2017.